Chapter 5
Tsunami Generation

Abstract This chapter theoretically investigates tsunami generation. When an earthquake occurs in an offshore region, seismic waves, ocean acoustic waves, and tsunami are excited. Although the compressibility and elasticity of the sea layer are important for the propagation of ocean acoustic waves and high-frequency seismic waves, we may assume that the sea layer is incompressible for tsunami. This chapter is based on incompressible fluid dynamics. The theory gives the analytical solutions for tsunami generation and propagation, by which we would be able to understand the mechanism behind these phenomena in addition to describing the motion. Section 5.1 explains the difference between ocean acoustic waves and tsunami. In Sect. 5.2, a linear potential theory is formulated for the tsunami generation process in a water with uniform depth. Analytical solutions for the sea-surface displacement, velocity, and pressure field in the seawater are derived. In Sect. 5.3, we examine the analytical solutions for tsunami generation and propagation. The mathematical equations can directly provide us with a clear perspective on the tsunami mechanism. In Sect. 5.4, we bridge the gap between the analytical solutions derived under a constant sea-depth assumption and tsunami simulations with realistic bathymetry. The theoretical background of the initial conditions in the numerical simulations is explained.

Keywords Linear potential theory · Incompressible fluid · Initial tsunami height distribution · Dynamic pressure change · Static pressure change

5.1 Ocean Acoustic Waves and Tsunami: Different Driving Forces

Earthquakes excite seismic waves and tsunami. Seawater is characterized by zero rigidity. In other words, shear stress is zero in the sea, even if shear strain is considerably large. As a result, the S wave that is excited by shear stress cannot propagate through the sea layer. Only the P wave can propagate through the sea layer. The ocean acoustic wave is nothing but the P wave trapped within the sea layer

T. Saito, *Tsunami Generation and Propagation*, Springer Geophysics,
https://doi.org/10.1007/978-4-431-56850-6_5

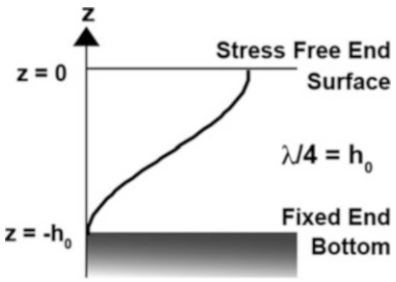

Fig. 5.1 A simple model for a fundamental mode in a region bounded by a free end and a fixed end

from the viewpoint of elastic wave theory. If the period is longer, the *P* wave wavelength becomes longer, which results in the energy extending significantly into the crust. The wave may be considered as a seismic *P* wave rather than an ocean acoustic wave, because the restoring force of the wave is mainly caused by the elasticity of the crust rather than the water layer.

Let us roughly estimate the longest period of the ocean acoustic waves. When the phase velocity of the ocean acoustic wave is c_0 and the period is T_0, the wavelength is given by $\lambda = c_0 T_0$. Assuming a boundary condition at the sea surface as a stress-free boundary and one at the sea bottom as a rigid boundary (fixed end), the fundamental mode of the ocean acoustic wave is given by $\lambda/4 = h_0$ where h_0 is the sea depth (Fig. 5.1). This gives the period of the ocean acoustic wave as $T_0 = 4h_0/c_0$. This is the period of the fundamental mode or the mode of the longest period in this system. When considering the average depth of the Pacific Ocean to be $h_0 = 4000$ m and the ocean acoustic wave velocity to be $c_0 = 1.5$ km/s, then the period is $T_0 \sim 10$ s. This indicates that the period of the ocean acoustic wave should be shorter than $T_0 < \sim 10$ s so that the *P* wave is trapped within the sea layer. When the sea depth becomes smaller, the characteristic period becomes smaller. If the sea depth is $h_0 = 1000$ m, the characteristic time is $T_0 \sim 2.5$s. The derivation here is a very simple one. Section 3.3.2 *Ocean Acoustic Waves* describes the theory of ocean acoustic waves and their critical time based on a more general approach.

We then consider tsunami. Near the earthquake fault, the fault slip causes permanent displacement. The gravity collapses the permanent displacement of the sea surface as shown in Fig. 5.2. The sea layer cannot keep the displacement distribution (deformation) at the sea surface since the water layer does not hold shear stress. As a result, the water volume uplifted by the earthquake flows downward. This downward flow of large volume of water causes long-wavelength horizontal flow in the sea layer from the bottom to the surface. This volume fluctuation propagates a long distance as a tsunami. Apparently, the main force causing the tsunami is gravity. The tsunami propagation velocity is roughly given by $\sqrt{g_0 h_0}$ when the wavelength is much longer than the sea depth (Chap. 3). If we consider the tsunami wavelength to be $\lambda = 100$ km and $h_0 = 4000$ m, the dominant period is $T_0 = \lambda/\sqrt{g_0 h_0} \sim 500$ s.

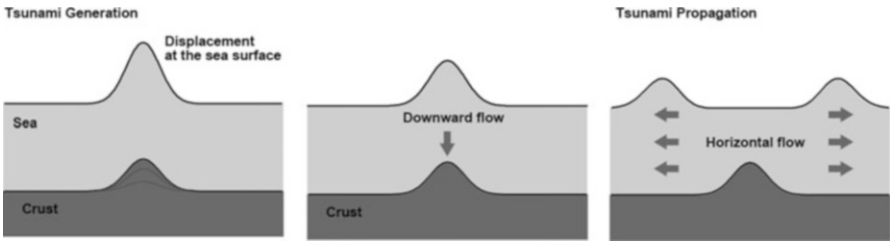

Fig. 5.2 A schematic illustration of tsunami generation and propagation

As stated above, earthquakes excite both ocean acoustic waves and tsunami. Note that both ocean acoustic waves and tsunami produce the sea-surface displacement. However, the excitation mechanisms are totally different. The difference originates from the restoring force. The seismic wave (ocean acoustic wave) requires the seawater to exhibit elasticity. Tsunami propagation requires gravity as a restoring force. As a consequence, the time scale (the dominant period) of the tsunami is often longer than ~10 min, which is much longer than that of the ocean acoustic wave < ~10 s. This substantial difference in the time scales allows us to consider the tsunami and ocean acoustic waves separately in many practical cases. Section 4.3.2*: Seismic Waves, Ocean Acoustic Waves, and Permanent Displacement* described the seismic wave propagation in elastic media. This chapter considers tsunami.

5.2 Linear Potential Theory

The tsunami generation process is described by a linear incompressible fluid theory in which the elasticity or compressibility of the seawater is neglected. Considering appropriate boundary conditions at the sea surface using the gravitational acceleration g_0 and giving the sea bottom displacement as a source of the tsunami, the tsunami generation theory describes the water motion in the sea layer. A solution represented in the wavenumber-frequency domain was found in Takahashi (1942) for the case of a constant sea depth. Kajiura (1963) derived an analytical solution for the vertical displacement at the sea surface caused by instantaneous sea-bottom deformation (i.e., the sea-bottom displacement represented by a step function with respect to time). The analytical solution is often referred to as Kajiura's equation, which is frequently used in the setting of the initial tsunami height distribution for tsunami propagation simulations (e.g., Tanioka and Seno 2001). The solutions are applicable just after the sea-bottom deformation ends but cannot describe the wavefield in the sea layer during the generation (e.g., Kervella et al. 2007). Saito (2013) derived more general solutions, which can describe the water particle motion through the sea layer during the tsunami generation. In the following sections, the theory is illustrated.

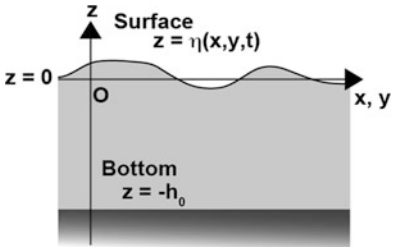

Fig. 5.3 Coordinates used in the formulation

5.2.1 Governing Equations

Cartesian coordinates (Fig. 5.3) are used for the formulation. The z-axis runs vertically upward, and the x- and y-axes lie in a horizontal plane. The sea surface at rest is located at $z = 0$, and the flat sea bottom is at $z = -h_0$. The sea-surface height is given by $z = \eta\ (x, y, t)$.

The particle velocity in the fluid is given by the vector $\mathbf{v}\ (\mathbf{x}, t) = v_x\mathbf{e_x} + v_y\mathbf{e_y} + v_z\mathbf{e_z}$ where $\mathbf{x} = x\mathbf{e_x} + y\mathbf{e_y} + z\mathbf{e_z}$ and $\mathbf{e_x}$, $\mathbf{e_y}$, and $\mathbf{e_z}$ are the basis unit vectors in the x-, y-, and z-axes, respectively. The sea-surface height $\eta(x, y, t)$ is assumed to be small enough compared with the water depth, i.e., $|\eta| \ll h_0$. An incompressible medium does not allow dilatation as

$$\nabla \cdot \mathbf{v} = 0. \tag{5.1}$$

When an irrotational flow is assumed (rot $\mathbf{v}(\mathbf{x}, t) = 0$), the velocity vector is represented using the velocity potential $\phi(\mathbf{x}, t)$ as

$$\mathbf{v}(\mathbf{x}, t) = \nabla\phi(\mathbf{x}, t). \tag{5.2}$$

Substitution of Eq. (5.2) into Eq. (5.1) gives

$$\Delta\phi(\mathbf{x}, t) = 0. \tag{5.3}$$

In an incompressible medium, the velocity potential $\phi(\mathbf{x}, t)$ needs to satisfy the Laplace equation.

We then consider the equation of motion in the sea layer. The linear equation of motion is given by

$$\frac{\partial \mathbf{v}(\mathbf{x}, t)}{\partial t} = -\frac{1}{\rho_0}\nabla p(\mathbf{x}, t) + \mathbf{g}_0, \tag{5.4}$$

where ρ_0 is the water density that is assumed to be constant, $p(\mathbf{x}, t)$ is the pressure, and $\mathbf{g}_0$ is the body force due to gravity. This equation is also derived if we assume a

constant density through the medium and a shear-wave velocity or rigidity of zero in the equation for the elastic medium (Eqs. (3.14) and (3.29)).

Consider a case when the pressure field is independent of time, that is, when the water is static or in an equilibrium state. Equation (5.4) becomes

$$0 = -\frac{1}{\rho_0}\nabla p_0(\mathbf{x}) + \mathbf{g}_0. \tag{5.5}$$

The pressure $p_0(\mathbf{x})$ is referred to as hydrostatic pressure. The pressure $p(\mathbf{x}, t)$ in Eq. (5.4) is represented by the sum of the hydrostatic pressure $p_0(\mathbf{x})$ and the fluctuation $p_e(\mathbf{x}, t)$ caused by the fluid motion as

$$p(\mathbf{x}, t) = p_0(\mathbf{x}) + p_e(\mathbf{x}, t). \tag{5.6}$$

Substituting Eq. (5.6) into (5.4) and using Eq. (5.5) gives the following equation

$$\begin{aligned}\frac{\partial \mathbf{v}(\mathbf{x}, t)}{\partial t} &= -\frac{1}{\rho_0}\nabla p_0(\mathbf{x}) - \frac{1}{\rho_0}\nabla p_e(\mathbf{x}, t) + \mathbf{g}_0 \\ &= -\frac{1}{\rho_0}\nabla p_e(\mathbf{x}, t).\end{aligned}$$

Then, using Eq. (5.2), we obtain

$$\nabla \frac{\partial \phi(\mathbf{x}, t)}{\partial t} = -\frac{1}{\rho_0}\nabla p_e(\mathbf{x}, t).$$

Since that $p_e(\mathbf{x}, t)$ should be zero when the system is in an equilibrium state, the pressure due to the motion $p_e(\mathbf{x}, t)$ is represented by the velocity potential $\phi(\mathbf{x}, t)$ as

$$p_e(\mathbf{x}, t) = -\rho_0 \frac{\partial \phi(\mathbf{x}, t)}{\partial t}. \tag{5.7}$$

Let us consider the boundary condition of the velocity potential $\phi(\mathbf{x}, t)$ at the sea surface $z = 0$. The vertical displacement at the surface $\eta(x, y, t)$ is given by an integration of the vertical velocity at the surface as

$$\eta(x, y, t) = \int_{-\infty}^{t} v_z(x, y, z = 0, t)dt.$$

By using the velocity potential (5.2), the surface $\eta(x, y, t)$ is represented as

$$\eta(x,y,t) = \int_{-\infty}^{t} \left.\frac{\partial \phi(\mathbf{x},t)}{\partial z}\right|_{z=0} dt. \tag{5.8}$$

Differentiating Eq. (5.8) with respect to time gives

$$\frac{\partial \eta(x,y,t)}{\partial t} = \left.\frac{\partial \phi(\mathbf{x},t)}{\partial z}\right|_{z=0}. \tag{5.9}$$

This represents the relation between the motion and the shape of the surface. It is referred to as the kinematic boundary condition.

We then consider the pressure at the surface. When the sea-surface height is $\eta(x, y, t)$, the pressure at $z = 0$ is given by $p_e(z = 0) = \rho_0 g_0 \eta(x, y, t)$ (Eq. (3.34)). Considering that the pressure is represented by the velocity potential in Eq. (5.7), the velocity potential satisfies

$$-\left.\frac{\partial \phi(\mathbf{x},t)}{\partial t}\right|_{z=0} = g_0 \eta(x,y,t), \tag{5.10}$$

at $z = 0$. Since this condition is related to the motion and the force (pressure), this is referred to as the dynamic boundary condition. By using kinematic and dynamic boundary conditions (Eqs. (5.9) and (5.10)) and deleting the surface height $\eta(x, y, t)$, we obtain

$$\left.\frac{\partial^2 \phi(\mathbf{x},t)}{\partial t^2}\right|_{z=0} + g_0 \left.\frac{\partial \phi(\mathbf{x},t)}{\partial z}\right|_{z=0} = 0, \tag{5.11}$$

as the boundary condition of the velocity potential $\phi(\mathbf{x}, t)$ at the surface. The boundary condition of Eq. (5.11) at the sea surface is common in fluid dynamics (e.g., Kambe 2007; Pedlosky 2013).

Then, we consider the boundary condition at the sea bottom ($z = -h_0$). In many fluid dynamic problems, assuming the continuity of the vertical displacement on a rigid sea bottom, the vertical velocity is set as zero at the sea bottom. This is a boundary condition for the propagation problem. On the other hand, in the tsunami generation problem, we describe the motion at the sea bottom as the tsunami source (e.g., Takahashi 1942). Supposing the permanent vertical displacement at the sea bottom is given by $d(x, y)$, the vertical velocity at the sea bottom is represented as $d(x, y)\chi(t)$, where a function $\chi(t)$ has a dimension of inverse of the time. The function $\chi(t)$ represents the time evolution of the displacement at the bottom. Since it represents the rate of sea-bottom displacement, we refer to $\chi(t)$ as the rate function. The boundary condition of the velocity potential at the bottom is given by

$$v_z(x, y, z = -h_0, t) = \left.\frac{\partial \phi(\mathbf{x}, t)}{\partial z}\right|_{z=-h_0} = d(x, y)\chi(t). \tag{5.12}$$

The rate function $\chi(t)$ needs to satisfy

$$\int_{-\infty}^{\infty} \chi(t)dt = 1. \tag{5.13}$$

For example, when the sea-bottom deformation occurs with an infinitely short duration time at $t = 0$, the function $\chi(t)$ is given by the delta function:

$$\chi(t) = \delta(t). \tag{5.14}$$

On one hand, the sea-bottom deformation occurs during the finite duration t_c, which is closely related to the rise time in the earthquake fault motion. The function $\chi(t)$ is, for example, given by

$$\chi(t) = \frac{1}{\sqrt{\pi}}\frac{4}{t_c}\exp\left[-\left(\frac{t - t_0}{t_c/4}\right)^2\right], \tag{5.15}$$

where t_c determines the duration and t_0 controls the time when the deformation rate reaches its maximum. Figure 5.4a shows the function $\chi(t)$ when $t_c = 40$ s and $t_0 = 30$ s.

We have listed all the ingredients of the tsunami generation formulation. The wave motion $\mathbf{v}(\mathbf{x}, t)$ and the pressure field $p_e(\mathbf{x}, t)$ can be described by Eqs. (5.2) and (5.7), respectively, using the velocity potential $\phi(\mathbf{x}, t)$. The velocity potential $\phi(\mathbf{x}, t)$ satisfies the Laplace equation (Eq. (5.3)) through the water medium. The boundary conditions at the surface and the bottom are given by Eqs. (5.11) and (5.12), respectively. To find the solution of the velocity potential that satisfies Eqs. (5.3), (5.11), and (5.12) is a mathematical problem in the study of tsunami generation and propagation.

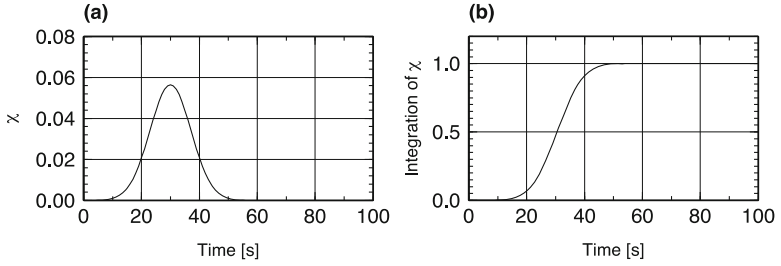

Fig. 5.4 (**a**) A rate function $\chi(t)$ and (**b**) an integration of $\chi(t)$ with respect to time t. The parameters are set at $t_c = 40$ s and $t_0 = 30$ s in Eq. (5.15)

5.2.2 Solving Laplace Equation with Boundary Conditions

By taking the 2-D Fourier transform in space-wavenumber domain and the Fourier transform in time-angular frequency domain, we transform $\phi(x, y, z, t)$ to $\widehat{\phi}\left(k_x, k_y, z, \omega\right)$ as,

$$\widehat{\phi}\left(k_x, k_y, z, \omega\right) = \int \int_{-\infty}^{\infty} dxdy \int_{-\infty}^{\infty} dt\, e^{-i\left(k_x x + k_y y\right)} e^{i\omega t} \phi(x, y, z, t). \tag{5.16}$$

The corresponding inverse Fourier transform is

$$\phi(x, y, z, t) = \frac{1}{(2\pi)^2} \int \int_{-\infty}^{\infty} dk_x dk_y \frac{1}{2\pi} \int_{-\infty}^{\infty} d\omega\, e^{i\left(k_x x + k_y y\right)} e^{-i\omega t} \widehat{\phi}\left(k_x, k_y, z, \omega\right). \tag{5.17}$$

By using this definition of the Fourier transform, we rewrite the Laplace equation (Eq. (5.3)) as

$$\frac{d^2}{dz^2} \widehat{\phi}\left(k_x, k_y, z, \omega\right) = k^2 \widehat{\phi}\left(k_x, k_y, z, \omega\right), \tag{5.18}$$

where $k^2 = {k_x}^2 + {k_y}^2$. Since, in Eq. (5.18), the values of k_x, k_y, and ω are considered to be constant values rather than independent variables, we used a representation of d/dz instead of $\partial/\partial z$. A general solution of this ordinary differential equation of (5.18) is given by

$$\widehat{\phi}\left(k_x, k_y, z, \omega\right) = A \cosh(kz) + B \sinh(kz). \tag{5.19}$$

The coefficients A and B should be chosen so as to satisfy the boundary conditions.

The boundary condition at the surface (Eq. (5.11)) is given by

$$\left(\frac{d}{dz} - \frac{\omega^2}{g_0}\right) \widehat{\phi}\left(k_x, k_y, z, \omega\right)\Big|_{z=0} = 0, \tag{5.20}$$

and that at the bottom (Eq. (5.12)) is given by

$$\frac{d}{dz} \widehat{\phi}\left(k_x, k_y, z, \omega\right)\Big|_{z=-h_0} = \widehat{d}\left(k_x, k_y\right) \widehat{\chi}(\omega), \tag{5.21}$$

in the wavenumber-angular frequency domain when the Fourier transform (Eq. (5.16)) is used, where $\widehat{d}\left(k_x, k_y\right)$ is the 2-D spatial Fourier transform of $d(x, y)$ and $\widehat{\chi}(\omega)$ is the Fourier transform of $\chi(t)$.

Substituting Eq. (5.19) into Eq. (5.20) and Eq. (5.21) gives

$$-\frac{\omega^2}{g_0}A + kB = 0,$$

and

$$-kA\sinh kh_0 + kB\cosh kh_0 = \widehat{d}\left(k_x, k_y\right)\widehat{\chi}(\omega).$$

Then, the coefficients A and B are given by

$$A = \frac{1}{(k\omega^2/g_0)\cosh kh_0 - k^2\sinh kh_0}k\widehat{d}\left(k_x, k_y\right)\widehat{\chi}(\omega),$$

and

$$B = \frac{1}{(k\omega^2/g_0)\cosh kh_0 - k^2\sinh kh_0}\frac{\omega^2}{g_0}\widehat{d}\left(k_x, k_y\right)\widehat{\chi}(\omega).$$

By substituting the estimated A and B into Eq. (5.19), we obtain

$$\widehat{\phi}\left(k_x, k_y, z, \omega\right) = \frac{1}{k}\frac{\omega^2\sinh(kz) + g_0k\cosh(kz)}{\omega^2\cosh(kh_0) - g_0k\sinh(kh_0)}\widehat{d}\left(k_x, k_y\right)\widehat{\chi}(\omega). \tag{5.22}$$

We then obtain a solution in time and space by the inverse Fourier transform as follows:

$$\begin{aligned}\phi(x, y, z, t) = \frac{1}{2\pi}\int_{-\infty}^{\infty} e^{-i\omega t}\widehat{\chi}(\omega)d\omega\frac{1}{(2\pi)^2}\int_{-\infty}^{\infty}\int_{-\infty}^{\infty} dk_x dk_y\, e^{i\left(k_x x + k_y y\right)} \\ \frac{1}{k}\frac{\omega^2\sinh(kz) + g_0k\cosh(kz)}{\omega^2\cosh(kh_0) - g_0k\sinh(kh_0)}\widehat{d}\left(k_x, k_y\right).\end{aligned} \tag{5.23}$$

This is a formal expression of the velocity potential using the inverse Fourier transform. This formal expression was shown in Takahashi (1942) using cylindrical coordinates. This form is still not suitable for examining the mechanism of the tsunami generation process. If the integration of the angular frequency ω were performed, we would be able to interpret the analytical solution in order to understand the mechanism of tsunami generation and propagation. The main difficulty with respect to the integration of the angular frequency ω is that the residue theorem is not applicable when $\chi(t)$ is an arbitrary function or is given by the delta function $\chi(t) = \delta(t)$.

In order to conduct the integration with respect to the angular frequency using the residue theorem, we first consider a special case in which the rate function $\chi(t)$ is represented as

$$\chi(t) = \begin{cases} \dfrac{1}{T} & \text{for } 0 < t < T \\ 0 & \text{for others} \end{cases} = \frac{1}{T}[H(t) - H(t-T)], \tag{5.24}$$

where a function $H(t)$ is defined as

$$H(t) = \begin{cases} 0 & \text{for } t \le 0 \\ 1 & \text{for } t > 0. \end{cases} \tag{5.25}$$

The Fourier transform of the rate function is given by

$$\widehat{\chi}(\omega) = \int_{-\infty}^{\infty} \chi(t) e^{i\omega t} dt = \frac{1}{i\omega T}\left(e^{i\omega T} - 1\right). \tag{5.26}$$

Substitution of Eq. (5.26) into Eq. (5.23) gives Eq. (5.27) and Eq. (5.28)

$$\begin{aligned} &\phi(x,y,z,t) \\ &= \frac{1}{(2\pi)^2}\int_{-\infty}^{\infty}\int_{-\infty}^{\infty} dk_x dk_y\, e^{i\left(k_x x + k_y y\right)} \frac{1}{k}\frac{\widehat{d}\left(k_x,k_y\right)}{\cosh(kh_0)} \\ &\qquad \frac{1}{2\pi T}\frac{i}{}\int_{-\infty}^{\infty} d\omega\, e^{-i\omega t}\frac{1-e^{i\omega T}}{\omega}\frac{\omega^2\sinh(kz) + g_0 k\cosh(kz)}{\omega^2 - g_0 k\tanh(kh_0)} \\ &= \frac{1}{(2\pi)^2}\int_{-\infty}^{\infty}\int_{-\infty}^{\infty} dk_x dk_y\, e^{i\left(k_x x + k_y y\right)} \frac{1}{k}\frac{\widehat{d}\left(k_x,k_y\right)}{\cosh(kh_0)} \\ &\quad \frac{1}{2\pi T}\frac{i}{}\left[\int_{-\infty}^{\infty} d\omega \frac{e^{-i\omega t}}{\omega}\frac{\omega^2\sinh(kz) + g_0 k\cosh(kz)}{\omega^2 - g_0 k\tanh(kh_0)}\right. \\ &\qquad \left. - \int_{-\infty}^{\infty} d\omega \frac{e^{-i\omega(t-T)}}{\omega}\frac{\omega^2\sinh(kz) + g_0 k\cosh(kz)}{\omega^2 - g_0 k\tanh(kh_0)}\right]. \end{aligned} \tag{5.27}$$

We perform an integration with respect to ω by using the residue theorem in the complex ω plane by recognizing that the poles are located at $\omega = 0, \pm\sqrt{g_0 k\tanh(kh_0)}$ (Fig. 5.5). The detailed procedure is illustrated in Appendix 5A. The result of the integrations is

$$\begin{aligned} &\phi(x,y,z,t) \\ &= -\frac{1}{(2\pi)^2}\int_{-\infty}^{\infty}\int_{-\infty}^{\infty} dk_x dk_y\, e^{i\left(k_x x + k_y y\right)} \frac{\widehat{d}\left(k_x,k_y\right)}{k} \\ &\quad \left[\frac{\cosh(kz)}{\sinh(kh_0)}\frac{H(t-T) - H(t)}{T}\right. \\ &\qquad \left. - \left(\frac{\cosh(kz)}{\sinh(kh_0)} + \frac{\sinh(kz)}{\cosh(kh_0)}\right)\frac{H(t)\cos\left(\omega_0 t\right) - H(t-T)\cos\left(\omega_0(t-T)\right)}{T}\right], \end{aligned} \tag{5.28}$$

where the angular frequency ω_0 is given by

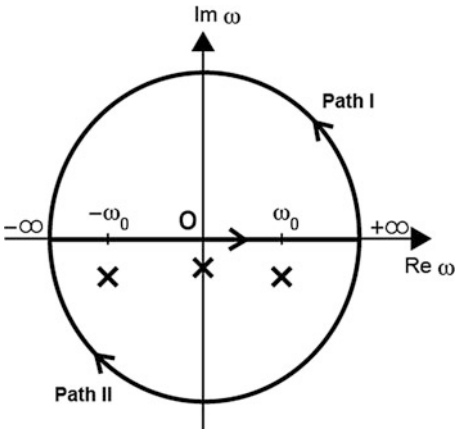

Fig. 5.5 Poles in the complex ω plane for tsunami generation and propagation

$$\omega_0 = \sqrt{g_0 k \tanh(kh_0)}. \tag{5.29}$$

Equation (5.29) is the dispersion relation of ocean waves propagating using gravity as the restoring force (see Eq. (3.47)).

Now, defining a function $\psi(x, y, z, t)$ as

$$\psi(x,y,z,t) = -\frac{1}{(2\pi)^2}\int_{-\infty}^{\infty}\int_{-\infty}^{\infty} dk_x dk_y\, e^{i\left(k_x x + k_y y\right)} \frac{\widehat{d}\left(k_x, k_y\right)}{k} \left[\frac{\cosh(kz)}{\sinh(kh_0)} - \left(\frac{\cosh(kz)}{\sinh(kh_0)} + \frac{\sinh(kz)}{\cosh(kh_0)}\right)\cos\left(\omega_0 t\right)\right] H(t), \tag{5.30}$$

we rewrite Eq. (5.28) as

$$\phi(x,y,z,t) = \frac{\psi(x,y,z,t) - \psi(x,y,z,t-T)}{T}. \tag{5.31}$$

Equations (5.30) and (5.31) represent the velocity potential for the sea-bottom deformation when the rate function of the sea-bottom deformation is given by a special form of Eq. (5.24).

5.2.2.1 Impulse Response

We then consider a general solution of the velocity potential for any rate function. When T approaches zero in Eq. (5.24), the rate function $\chi(t)$ approaches the delta function as

$$\chi(t) = \lim_{T\to 0} \frac{H(t) - H(t-T)}{T} = \delta(t). \tag{5.32}$$

Therefore, we obtain the velocity potential for the delta function type rate function (or impulsive rate function) by making T approach zero in Eq. (5.31). The corresponding velocity potential function $\phi_{\text{impulse}}(t)$ is given by

$$\phi_{\text{Impulse}}(\mathbf{x}, t) = \lim_{T\to 0} \frac{\psi(\mathbf{x}, t) - \psi(\mathbf{x}, t-T)}{T} = \frac{\partial \psi(\mathbf{x}, t)}{\partial t}. \tag{5.33}$$

Substituting Eq. (5.30) into Eq. (5.33), we obtain

$$\begin{aligned}
&\phi_{\text{Impulse}}(\mathbf{x}, t) \\
&\quad = \frac{\partial \psi(\mathbf{x}, t)}{\partial t} \\
&\quad = -\frac{1}{(2\pi)^2} \int_{-\infty}^{\infty} \int_{-\infty}^{\infty} dk_x dk_y \, e^{i\left(k_x x + k_y y\right)} \frac{\widehat{d}\left(k_x, k_y\right)}{k} \left[\frac{\cosh(kz)}{\sinh(kh_0)} \delta(t) \right. \\
&\qquad\qquad + \left(\frac{\cosh(kz)}{\sinh(kh_0)} + \frac{\sinh(kz)}{\cosh(kh_0)} \right) \omega_0 \sin\left(\omega_0 t\right) H(t) \\
&\qquad\qquad \left. - \left(\frac{\cosh(kz)}{\sinh(kh_0)} + \frac{\sinh(kz)}{\cosh(kh_0)} \right) \cos\left(\omega_0 t\right) \delta(t) \right] \\
&\quad = -\frac{1}{(2\pi)^2} \int_{-\infty}^{\infty} \int_{-\infty}^{\infty} dk_x dk_y \, e^{i\left(k_x x + k_y y\right)} \frac{\widehat{d}\left(k_x, k_y\right)}{k} \left[\frac{\cosh(kz)}{\sinh(kh_0)} \delta(t) \right. \\
&\qquad\qquad + \left(\frac{\cosh(kz)}{\sinh(kh_0)} + \frac{\sinh(kz)}{\cosh(kh_0)} \right) \omega_0 \sin\left(\omega_0 t\right) H(t) \\
&\qquad\qquad \left. - \left(\frac{\cosh(kz)}{\sinh(kh_0)} + \frac{\sinh(kz)}{\cosh(kh_0)} \right) \delta(t) \right],
\end{aligned}$$

where we set $t = 0$ in the term including $\delta(t)$. We calculate using a trigonometric sum identity as

$$\begin{aligned}
&\phi_{\text{Impulse}}(\mathbf{x}, t) \\
&= \frac{1}{(2\pi)^2} \int_{-\infty}^{\infty} \int_{-\infty}^{\infty} dk_x dk_y \, e^{i\left(k_x x + k_y y\right)} \frac{\widehat{d}\left(k_x, k_y\right)}{\cosh(kh_0)} \\
&\quad \left\{ -\frac{\omega_0}{k} \left[\cosh(kz) \frac{\cosh(kh_0)}{\sinh(kh_0)} + \sinh(kz) \right] \sin\left(\omega_0 t\right) H(t) + \frac{1}{k} \sinh(kz) \delta(t) \right\} \\
&= \frac{1}{(2\pi)^2} \int_{-\infty}^{\infty} \int_{-\infty}^{\infty} dk_x dk_y \, e^{i\left(k_x x + k_y y\right)} \frac{\widehat{d}\left(k_x, k_y\right)}{\cosh(kh_0)} \\
&\quad \left\{ -\frac{\omega_0}{k} \frac{\cosh[k(z + h_0)]}{\sinh kh_0} \sin\left(\omega_0 t\right) H(t) + \frac{1}{k} \sinh(kz) \delta(t) \right\}.
\end{aligned} \tag{5.34}$$

Equation (5.34) is the solution of the velocity potential with respect to the delta function or the impulse response. The solution with respect to any rate function $\chi(t)$ is given by the convolution:

$$\phi(\mathbf{x},t) = \int_{-\infty}^{\infty} \phi_{\text{Impulse}}(\mathbf{x}, t-\tau)\chi(\tau)d\tau. \tag{5.35}$$

5.2.2.2 Velocity Field

Since we have obtained an analytical representation of the velocity potential (5.34), the velocity field is given by the gradient of the velocity potential (Eq. (5.2)). Using the horizontal gradient ∇_H defined as

$$\nabla_H = \frac{\partial}{\partial x}\mathbf{e_x} + \frac{\partial}{\partial y}\mathbf{e_y}, \tag{5.36}$$

the horizontal velocity vector $\mathbf{v}_H(\mathbf{x},t)$ is represented as the following equation

$$\begin{aligned}\mathbf{v}_H(\mathbf{x},t) &= \nabla_H \phi_{\text{Impulse}}(\mathbf{x},t)\\ &= \frac{1}{(2\pi)^2}\int_{-\infty}^{\infty}\int_{-\infty}^{\infty} dk_x dk_y\, e^{i(k_x x + k_y y)}\frac{\widehat{d}(k_x,k_y)}{\cosh(kh_0)}\\ &\quad \left\{-i\omega_0 \frac{\mathbf{k}_H}{k} f_H(k,z,h_0)\sin(\omega_0 t)H(t) + \frac{i\mathbf{k}_H}{k}\sinh(kz)\delta(t)\right\},\end{aligned} \tag{5.37}$$

where $\mathbf{k}_H$ is defined as $\mathbf{k}_H \equiv k_x\mathbf{e_x} + k_y\mathbf{e_y}$ and the function $f_H(k,z,h_0)$ is defined as

$$f_H(k,z,h_0) = \frac{\cosh[k(z+h_0)]}{\sinh(kh_0)}. \tag{5.38}$$

The vertical velocity $v_z(\mathbf{x},t)$ is represented as

$$\begin{aligned}v_z(\mathbf{x},t) &= \frac{\partial \phi_{\text{Impulse}}(\mathbf{x},t)}{\partial z}\\ &= \frac{1}{(2\pi)^2}\int_{-\infty}^{\infty}\int_{-\infty}^{\infty} dk_x dk_y\, e^{i(k_x x + k_y y)}\frac{\widehat{d}(k_x,k_y)}{\cosh(kh_0)}\\ &\quad \left\{-\omega_0 f_z(k,z,h_0)\sin(\omega_0 t)H(t) + \cosh(kz)\delta(t)\right\},\end{aligned} \tag{5.39}$$

where the function $f_z(k,z,h_0)$ is defined as

$$f_z(k,z,h_0)=\frac{\sinh[k(z+h_0)]}{\sinh(kh_0)}. \tag{5.40}$$

The functions $f_H(k,z,h_0)$ and $f_z(k,z,h_0)$ indicate the velocity-amplitude distributions for the horizontal and vertical components, respectively, at a depth z in a sea of a constant depth h_0. These velocity distributions are peculiar to the propagation process. The same functions appear in Eqs. (3.53) and (3.55) for the propagation problem in Chap. 3. The distribution functions will be explained later (Fig. 5.13).

The vertical displacement at the surface, or the tsunami height $\eta(x,y,t)$, is given by the velocity potential (see Eq. (5.10)) as

$$\begin{aligned}\eta(x,y,t)&=-\frac{1}{g_0}\frac{\partial\phi_{\text{Impulse}}(\mathbf{x},t)}{\partial t}\bigg|_{z=0}\\&=\frac{1}{(2\pi)^2}\int_{-\infty}^{\infty}\int_{-\infty}^{\infty}dk_xdk_y\,e^{i\left(k_xx+k_yy\right)}\frac{\widehat{d}\left(k_x,k_y\right)}{\cosh(kh_0)}\cos\left(\omega_0t\right)H(t).\end{aligned} \tag{5.41}$$

The pressure change due to the fluid motion $p_e(\mathbf{x},t)$ is represented by the velocity potential (Eq. (5.7)) as

$$\begin{aligned}&p_e(\mathbf{x},t)\\&=-\rho_0\frac{\partial\phi_{\text{Impulse}}(\mathbf{x},t)}{\partial t}\\&=\frac{1}{(2\pi)^2}\int_{-\infty}^{\infty}\int_{-\infty}^{\infty}dk_xdk_y\,e^{i\left(k_xx+k_yy\right)}\frac{\rho_0\widehat{d}\left(k_x,k_y\right)}{\cosh(kh_0)}\\&\quad\left\{\frac{\omega_0^2}{k}\frac{\cosh[k(z+h_0)]}{\sinh kh_0}\cos\left(\omega_0t\right)H(t)\right.\\&\qquad\left.+\frac{\omega_0}{k}\frac{\cosh[k(z+h_0)]}{\sinh kh_0}\sin\left(\omega_0t\right)\delta(t)-\frac{1}{k}\sinh(kz)\cdot\frac{d\delta(t)}{dt}\right\}.\end{aligned}$$

Using the dispersion relation $\omega_0^2=g_0k\tanh kh_0$ (Eq. (5.29)), we rewrite Eq. (5.42),

$$\begin{aligned}p_e(\mathbf{x},t)=\;&\frac{1}{(2\pi)^2}\int_{-\infty}^{\infty}\int_{-\infty}^{\infty}dk_xdk_y\exp\left[i\left(k_xx+k_yy\right)\right]\\&\times\frac{\rho_0\widehat{d}\left(k_x,k_y\right)}{\cosh(kh_0)}\left\{g_0\frac{\cosh[k(z+h_0)]}{\cosh kh_0}\cos\left(\omega_0t\right)H(t)-\frac{1}{k}\sinh(kz)\cdot\frac{d\delta(t)}{dt}\right\}.\end{aligned} \tag{5.42}$$

In particular, the pressure change at the sea bottom $z=-h_0$ is given by Eq. (5.43)

$$\begin{aligned}p_e(\mathbf{x},t)|_{z=-h_0}=\;&\frac{1}{(2\pi)^2}\int_{-\infty}^{\infty}\int_{-\infty}^{\infty}dk_xdk_y\exp\left[i\left(k_xx+k_yy\right)\right]\\&\times\frac{\rho_0\widehat{d}\left(k_x,k_y\right)}{\cosh(kh_0)}\left\{g_0\frac{\cos\left(\omega_0t\right)}{\cosh(kh_0)}H(t)+\frac{1}{k}\sinh(kh_0)\cdot\frac{d\delta(t)}{dt}\right\}\end{aligned} \tag{5.43}$$

The analytical solutions of (5.37), (5.39), (5.41), and (5.42) describe the fluid and surface motion for the tsunami generation and propagation. It is noteworthy that only the tsunami height (Eq. (5.41)) is given by a single term that represents propagating waves characterized by the dispersion relation of Eq. (5.29). The particle velocity (Eqs. (5.37) and (5.39)) and the pressure (Eqs. (5.42) and (5.43)) are represented by the two terms. One of the terms represents propagating waves characterized by the dispersion relation of Eq. (5.29). The propagation term includes gravity acceleration g_0. The other term represents the contribution directly from the source. It is independent of gravity and does not represent the propagating waves. This term is necessary to reproduce the velocity and pressure field during the tsunami generation. The analytical solutions clearly indicate the generation process and the propagation process via the two different terms. Also, it is clear that gravity (g_0) plays an important role in the propagation, whereas the gravity does not appear in the generation. We will discuss the resultant equations in more detail in 5.3.2. *Analytical Solutions.*

5.3 Generation

5.3.1 Visualization

When computers were not sufficiently powerful, we relied mainly on analytical solutions to obtain images of wavefields. However, advances have made it possible for computers to visualize the wavefield, which greatly helps to our understanding tsunamis. By conducting an integration over the wavenumber (k_x, k_y) in Eqs. (5.37), (5.39), and (5.41) (a FFT subroutine is used for the integration), we can describe the spatial and temporal distribution of the velocity field and sea-surface height. As a simple example, sea-bottom motion is assumed to be given by the vertical velocity at $z = -h_0$ as

$$v_z(\mathbf{x}, t)|_{z=-h_0} = d_0 e^{-x^2/(L/2)^2} \frac{H(t) - H(t-T)}{T}, \tag{5.44}$$

where the permanent displacement at the sea bottom is given by $d(x, y) = d_0 \exp[-x^2/(L/2)^2]$ and the velocity does not change during the time T. The spatial Fourier transform (defined by Eq. (5.16)) of $d(x, y)$ is

$$\widehat{d}(k_x, k_y) = \frac{\sqrt{\pi} d_0 L}{2} e^{-(Lk_x)^2/16} \cdot 2\pi\delta(k_y),$$

where $\int_{-\infty}^{\infty} dy \exp(-iky) = 2\pi\delta(k_y)$ is used. Substituting $\widehat{d}(k_x, k_y)$ into Eqs. (5.37), (5.39), and (5.41) and convoluting the corresponding rate function, we describe the wavefield of tsunami generation. Discrete integration is conducted with respect to

the wavenumber k_x. We visualize two cases, large (long-wavelength) and small (short-wavelength) source area cases, in the following.

To represent a large source area generating long-wavelength tsunamis, we set the parameters in Eq. (5.44) as $d_0 = 1$ m, $L = 60$ km, and $T = 31$ s. This source region ($L = 60$ km) is sufficiently larger than the sea depth h_0 (=4 km). Figure 5.6 shows the height η (upper panel) and the velocity distribution in the sea (lower panel) for each elapsed time. As the sea bottom moves according to the boundary conditions in Eq. (5.44) ($T < 31$ s), it produces a vertical flow through the sea layer from the bottom to the surface over the source region (Fig. 5.6a, b, and c). The vertical flow uplifts the sea surface. When the sea-bottom motion ends ($T = 31$ s), the vertical velocity induced by the sea bottom disappears. The uplifted sea surface then begins to collapse, generating a descending flow (Fig. 5.6d). The descending water displaces a massive amount of water sideways from the source region, and the water moves with a dominant horizontal flow (Fig. 5.6e, f). The horizontal propagation of the displacement is the tsunami propagation. The horizontal velocity is always positive (negative) where the location x is positive (negative). These snapshots intuitively illustrate that gravity plays an important role in tsunami propagation. If gravity did not exist (or $g_0 = 0$), the uplifted sea surface would not collapse and the tsunami would not propagate.

We then consider a small source area generating short-wavelength tsunamis, setting the parameter $L = 20$ km, but the other parameters remain the same. The results are shown in Fig. 5.7. As the sea bottom moves ($T < 31$ s), the vertical velocity from the sea bottom produces a vertical flow of water over the source region (Fig. 5.7a, b, and c). Note that the maximum height at the surface (0.8 m) is smaller than in the case with a larger source ($L = 60$ km, Fig. 5.6). This indicates that the vertical velocity is less efficiently excited in a smaller source region. This is because the horizontal flow is more excited (see the flow vector around the sea bottom in Fig. 5.7a, b, and c). After the sea-bottom motion ends ($T > 31$ s), the collapse of the uplifted sea surface accelerates, which causes a descending flow (Fig. 5.7d). The descending water displaces the water sideways, and the water moves with a horizontal flow. Unlike the large source case where the horizontal flow dominates (Fig. 5.6), the vertical component of the velocity is also significant in Fig. 5.7e, f. The water height at the surface indicates a dispersive character: a short-wavelength tsunami propagates more slowly than a long-wavelength one. The horizontal component of the velocity distribution oscillates between positive and negative values. Prograde rotation of the velocity vector occurs near the surface. The velocity distribution accompanied by the short-wavelength tsunami is localized near the surface (Fig. 5.7f). This is because a short-wavelength tsunami cannot displace a large volume of water unlike a long-wavelength tsunami. The comparison of Figs. 5.6 and 5.7 shows that the tsunami generation and propagation characteristics strongly depend on the source size/depth ratio (60/4 and 20/4 in Figs. 5.6 and 5.7, respectively).

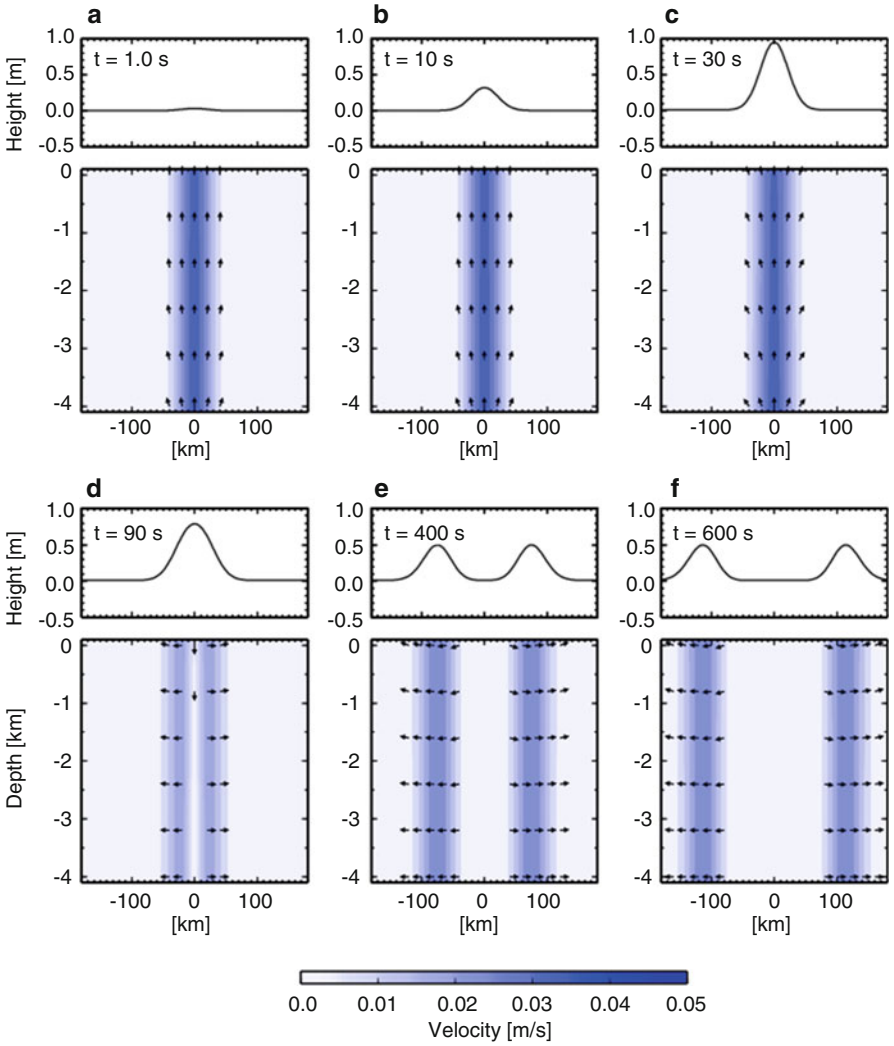

Fig. 5.6 Surface height and velocity distribution for a large source ($L = 60$ km). The permanent sea-bottom deformation is given by $d(x, y) = d_0 \exp[-x^2/(L/2)^2]$, where $d_0 = 1$ m, and the source duration is $T = 31$ s. The water height at the surface is shown in the upper panel, and the velocity distribution from the sea bottom to the sea surface is shown in the lower panel, for each elapsed time t from the start of sea-bottom deformation, (**a**) $t = 1$ s, (**b**) 10 s, (**c**) 30 s, (**d**) 90 s, (**e**) 400 s, and (**f**) 600 s. The vectors indicate the direction of the flow velocity in the fluid in the lower panel (Saito 2013, copyright by Springer)

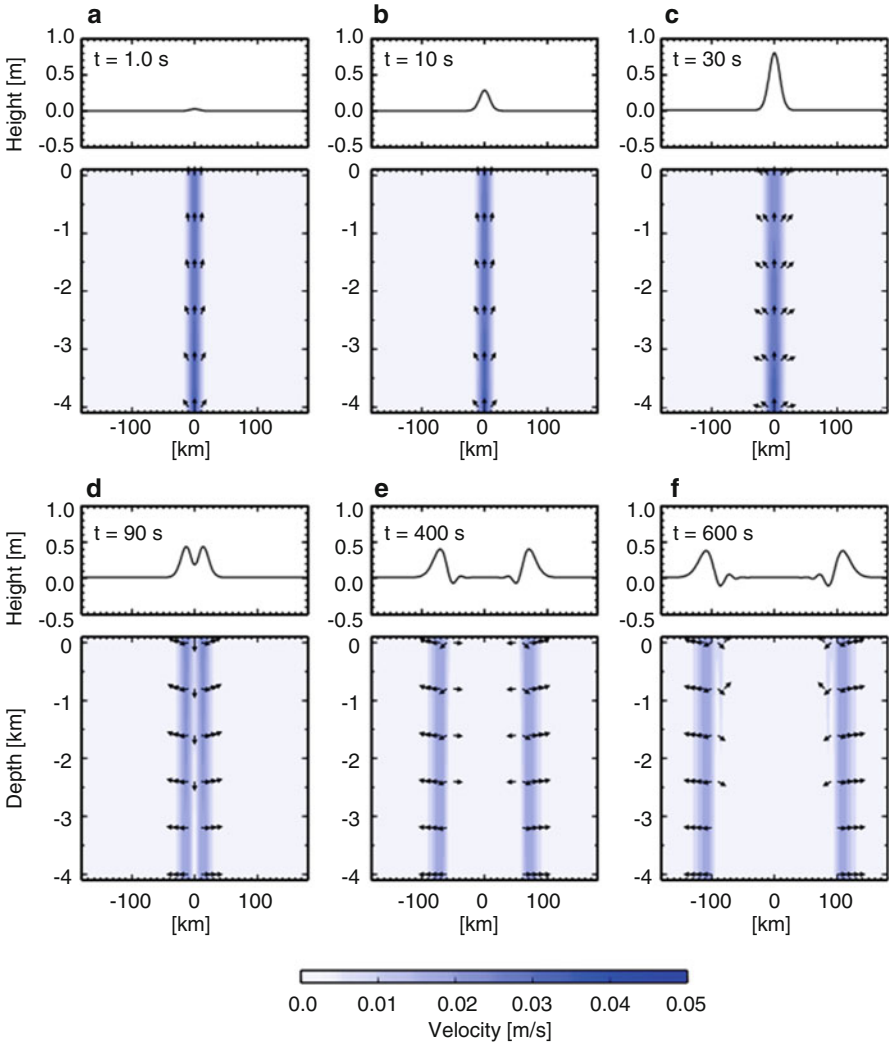

Fig. 5.7 Surface height and velocity distribution for a large source ($L = 20$ km). See Fig. 5.6 for details

5.3.2 *Analytical Solutions*

Then, we investigate tsunami generation and propagation by examining the analytical solutions (Eqs. (5.37), (5.39), and (5.41)).

5.3.2.1 Generation Process

We have considered tsunami generation to be caused by sea-bottom deformation. This is schematically shown in Fig. 5.8a. The resultant analytical solutions for the velocity potential, the horizontal components of the velocity field, the vertical component of the velocity field, the tsunami height, and the sea-bottom pressure change are listed again below.

$$\phi(t) = \frac{1}{(2\pi)^2}\int_{-\infty}^{\infty}\int_{-\infty}^{\infty} dk_x dk_y\, e^{i\left(k_x x + k_y y\right)}\frac{\widehat{d}\left(k_x, k_y\right)}{\cosh kh_0} \left\{-\frac{\omega_0}{k}\frac{\cosh[k(z+h_0)]}{\sinh kh_0}\sin\left(\omega_0 t\right)H(t) + \frac{1}{k}\sinh(kz)\delta(t)\right\}, \tag{5.45}$$

$$\mathbf{v}_H(\mathbf{x}, t) = \frac{1}{(2\pi)^2}\int_{-\infty}^{\infty}\int_{-\infty}^{\infty} dk_x dk_y\, e^{i\left(k_x x + k_y y\right)}\frac{\widehat{d}\left(k_x, k_y\right)}{\cosh kh_0} \left\{-i\omega_0\frac{\mathbf{k}_H}{k}\frac{\cosh[k(z+h_0)]}{\sinh kh_0}\sin\left(\omega_0 t\right)H(t) + \frac{i\mathbf{k}_H}{k}\sinh(kz)\delta(t)\right\}, \tag{5.46}$$

$$v_z(\mathbf{x}, t) = \frac{1}{(2\pi)^2}\int_{-\infty}^{\infty}\int_{-\infty}^{\infty} dk_x dk_y\, e^{i\left(k_x x + k_y y\right)}\frac{\widehat{d}\left(k_x, k_y\right)}{\cosh kh_0} \left\{-\omega_0\frac{\sinh[k(z+h_0)]}{\sinh kh_0}\sin\left(\omega_0 t\right)H(t) + \cosh(kz)\delta(t)\right\}, \tag{5.47}$$

$$\eta(x, y, t) = \frac{1}{(2\pi)^2}\int_{-\infty}^{\infty}\int_{-\infty}^{\infty} dk_x dk_y\, e^{i\left(k_x x + k_y y\right)}\frac{\widehat{d}\left(k_x, k_y\right)}{\cosh kh_0}\cos\left(\omega_0 t\right)H(t), \tag{5.48}$$

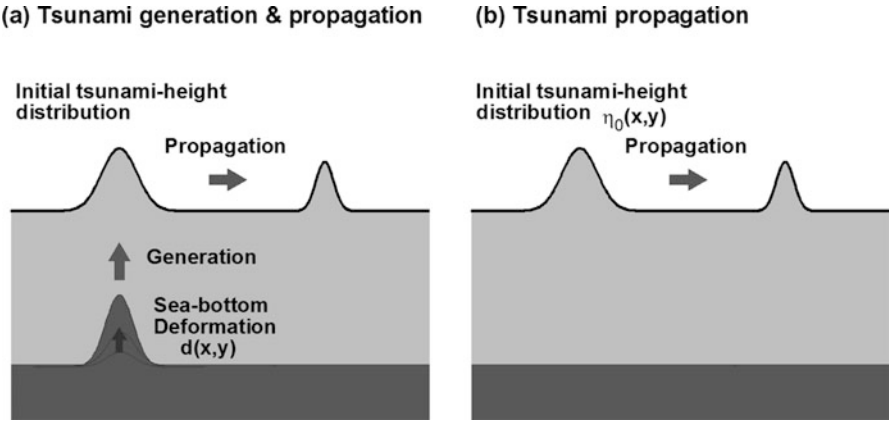

Fig. 5.8 (**a**) Tsunami generation due to sea-bottom deformation and its propagation. (**b**) Tsunami propagation from an initial tsunami height distribution (Saito 2013, copyright by Springer)

$$p_e(\mathbf{x},t)|_{z=-h_0} = \frac{1}{(2\pi)^2}\int_{-\infty}^{\infty}\int_{-\infty}^{\infty} dk_x dk_y\, e^{i\left(k_x x+k_y y\right)}\frac{\rho_0 \widehat{d}\left(k_x,k_y\right)}{\cosh kh_0} \left\{ g_0\frac{\cos\left(\omega_0 t\right)}{\cosh(kh_0)}H(t)+\frac{1}{k}\sinh(kh_0)\cdot\frac{d\delta(t)}{dt}\right\}. \tag{5.49}$$

In contrast to this situation, if we set the initial tsunami height distribution $\eta_0(x,y)$ as shown in Fig. 5.8b, we simulate only the propagation process without considering the generation process. By comparing these two cases (Fig. 5.8a, b) and investigating the difference, we can examine the generation process. The solutions obtained from the initial tsunami height distribution $\eta_0(x,y)$ are (Appendix 5B)

$$\phi_0(t) = \frac{1}{(2\pi)^2}\int_{-\infty}^{\infty}\int_{-\infty}^{\infty} dk_x dk_y\, e^{i\left(k_x x+k_y y\right)}\widehat{\eta}_0\left(k_x,k_y\right) \left\{-\frac{\omega_0}{k}\frac{\cosh[k(z+h_0)]}{\sinh kh_0}\sin\left(\omega_0 t\right)H(t)\right\}, \tag{5.50}$$

$$\mathbf{v}_H(\mathbf{x},t) = \frac{1}{(2\pi)^2}\int_{-\infty}^{\infty}\int_{-\infty}^{\infty} dk_x dk_y\, e^{i\left(k_x x+k_y y\right)}\widehat{\eta}_0\left(k_x,k_y\right) \left\{-i\omega_0\frac{\mathbf{k}_H}{k}\frac{\cosh[k(z+h_0)]}{\sinh kh_0}\sin\left(\omega_0 t\right)H(t)\right\}, \tag{5.51}$$

$$\mathrm{v}_z(\mathbf{x},t) = \frac{1}{(2\pi)^2}\int_{-\infty}^{\infty}\int_{-\infty}^{\infty} dk_x dk_y\, e^{i\left(k_x x+k_y y\right)}\widehat{\eta}_0\left(k_x,k_y\right) \left\{-\omega_0\frac{\sinh[k(z+h_0)]}{\sinh kh_0}\sin\left(\omega_0 t\right)H(t)\right\}, \tag{5.52}$$

$$\eta(\mathbf{x},t) = \frac{1}{(2\pi)^2}\int_{-\infty}^{\infty}\int_{-\infty}^{\infty} dk_x dk_y\, e^{i\left(k_x x+k_y y\right)}\widehat{\eta}_0\left(k_x,k_y\right)\cos\left(\omega_0 t\right)H(t), \tag{5.53}$$

$$p_e(x,y,z=-h_0,t) = \frac{1}{(2\pi)^2}\int_{-\infty}^{\infty}\int_{-\infty}^{\infty} dk_x dk_y\, e^{i\left(k_x x+k_y y\right)}\rho_0 g_0\widehat{\eta}_0\left(k_x,k_y\right)\frac{\cos\left(\omega_0 t\right)}{\cosh(kh_0)}H(t), \tag{5.54}$$

where $\widehat{\eta}_0\left(k_x,k_y\right)$ is the 2-D spatial Fourier transform of the initial tsunami height distribution $\eta_0(x,y)$.

5.3.2.2 Gravity

Comparison of the solutions with and without the generation process (e.g., a comparison of (5.45) and (5.50)) indicates that the generation process is described by the term represented by the delta function in Eqs. (5.45, 5.46, 5.47), and (5.49).

These terms do not contain the acceleration of gravity g_0. The generation process is basically independent of gravity. This is a fundamental feature of the generation process in contrast to the propagation process. This theoretical consequence supports the idea that the permanent sea-surface displacement calculated without considering gravity (e.g., Okada 1985) works as an initial tsunami height distribution. We also discuss the methods in 4.3.2 *Seismic Waves, Ocean Acoustic Waves, and Permanent Displacement*.

5.3.2.3 Factor of 1/ cosh (kh_0)

The factor $\widehat{d}(k_x, k_y)/\cosh(kh_0)$ appears in the generation process, while $\widehat{\eta}_0(k_x, k_y)$ appears in the solutions without the generation process. This suggests that the factor $\widehat{d}(k_x, k_y)/\cosh(kh_0)$ contains the information about the generation process. The initial tsunami height distribution caused by the sea-bottom deformation is not identical to the sea-bottom deformation. The factor 1/ cosh (kh_0) works as a spatial low-wavelength pass filter. This is often called Kajiura filter (Kajiura 1963). Figure 5.9 shows the factor 1/ cosh (kh_0). This filter removes the short-wavelength components ($k > 1/h_0$) as a low-wavelength pass filter. Due to this low-wavelength pass filter, the initial tsunami height distribution (sea-surface displacement distribution) becomes smooth.

Kajiura (1963) conducted the integration over the wavenumber domain and derived the analytical solution in the spatial domain as

$$\begin{aligned}\overline{\eta}(x, y, 0) &= \frac{1}{(2\pi)^2}\int_{-\infty}^{\infty}\int_{-\infty}^{\infty} dk_x dk_y\, e^{i(k_x x + k_y y)}\frac{1}{\cosh(kh_0)} \\ &= \frac{1}{2\pi}\int_0^{\infty} dk\, J_0(kr)\frac{k}{\cosh(kh_0)}.\end{aligned}$$

Using a series of exponential (Eq. (1.232.2) in Gradshteyn and Ryzihk 2000):

$$\frac{1}{\cosh x} = \operatorname{sech} x = 2\sum_{n=0}^{\infty}(-1)^n \exp[-(2n+1)x],$$

we obtain

$$\begin{aligned}\overline{\eta}(x, y, 0) &= \frac{1}{\pi}\sum_{n=0}^{\infty}(-1)^n \int_0^{\infty} dk \exp[-(2n+1)kh_0]k\, J_0(kr) \\ &= \frac{1}{\pi r^2}\sum_{n=0}^{\infty}(-1)^n \int_0^{\infty} d\bar{k} \exp\left[-(2n+1)\frac{h_0}{r}\bar{k}\right]\bar{k}\, J_0(\bar{k}).\end{aligned}$$

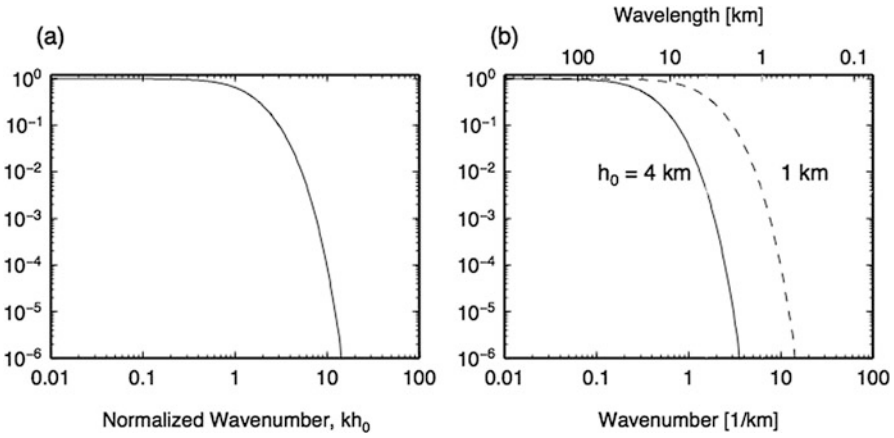

Fig. 5.9 (**a**) A function of $1/\cosh(kh_0)$ with respect to the normalized wavenumber kh_0 where k is the wavenumber of the sea-bottom deformation and h_0 is the sea depth. (**b**) A function of $1/\cosh(kh_0)$ with respect to the wavenumber k for the sea depth of $h_0 = 4$ km (solid line) and 1 km (dashed line). The function of $1/\cosh(kh_0)$ works as a low-wavelength pass filter that removes the high wavenumber components $k \gg 1/h_0$

The integration is conducted using a formula (Eq. (6.623.2) in Gradshteyn and Ryzihk 2000):

$$\int_0^\infty d\bar{k} \exp\left(-\bar{h}\bar{k}\right)\bar{k}\, J_0\left(\bar{k}\right) = \frac{\bar{h}}{\left(\bar{h}^2+1\right)^{3/2}}.$$

Then, we obtain

$$\begin{aligned}\overline{\eta}(x,y,0) &= \frac{1}{\pi r^2}\sum_{n=0}^{\infty}(-1)^n(2n+1)\frac{h_0}{r}\frac{1}{\left[(2n+1)^2(h_0/r)^2+1\right]^{3/2}} \\ &= \frac{1}{\pi h_0^2}\sum_{n=0}^{\infty}\frac{(-1)^n(2n+1)}{\left[(r/h_0)^2+(2n+1)^2\right]^{3/2}}.\end{aligned} \tag{5.55}$$

This is the vertical displacement distribution at the sea surface for the sea-bottom deformation occurring at a point given by $d_z(x,y) = \delta(x)\delta(y)$. Equation (5.55) is often referred to as Kajiura's equation (Kajiura 1963). Figure 5.10 shows Eq. (5.55) with respect to the distance normalized by the sea depth, r/h_0.

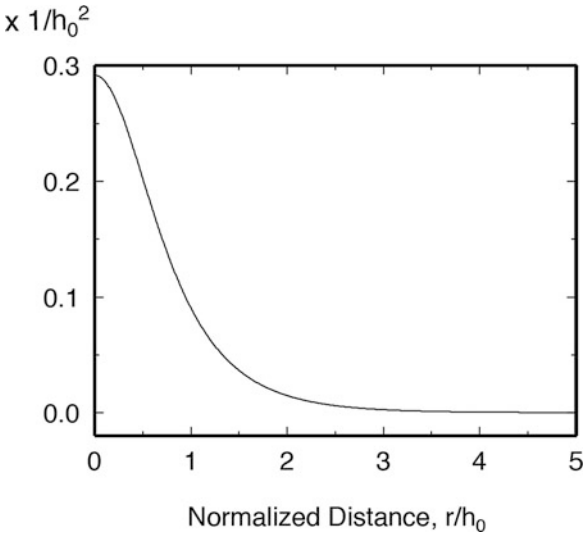

Fig. 5.10 Sea-surface height distribution with respect to the point source vertical displacement at the sea bottom given by $\delta(x)\delta(y)$. The distance r is given by $r = \sqrt{x^2 + y^2}$, and the sea depth is h_0

5.3.2.4 Conservation of Displaced Water Volume

When the sea-bottom displacement is given by $d(x, y)$, the total volume brought by the sea-bottom movement into the sea layer is given by the integral over 2-D horizontal space as

$$\begin{aligned}\int\int_{-\infty}^{\infty} d(x,y)dxdy &= \int\int_{-\infty}^{\infty} dxdy \frac{1}{(2\pi)^2} \int\int_{-\infty}^{\infty} dk_x dk_y \, \widehat{d}\left(k_x, k_y\right) e^{i\left(k_x x + k_y y\right)} \\ &= \int\int_{-\infty}^{\infty} dk_x dk_y \, \delta(k_x)\delta\left(k_y\right)\widehat{d}\left(k_x, k_y\right) \\ &= \widehat{d}(0,0).\end{aligned} \tag{5.56}$$

On the other hand, the total displaced water volume at the sea surface is given by

$$\begin{aligned}\int\int_{-\infty}^{\infty} \eta(x,y,0)dxdy &= \int\int_{-\infty}^{\infty} dxdy \frac{1}{(2\pi)^2} \int\int_{-\infty}^{\infty} dk_x dk_y \frac{\widehat{d}\left(k_x, k_y\right)}{\cosh(kh_0)} e^{i\left(k_x x + k_y y\right)} \\ &= \int\int_{-\infty}^{\infty} dk_x dk_y \, \delta(k_x)\delta\left(k_y\right) \frac{\widehat{d}\left(k_x, k_y\right)}{\cosh(kh_0)} \\ &= \widehat{d}(0,0).\end{aligned} \tag{5.57}$$

Even though the sea-surface height distribution $\eta(x, y, 0)$ has fewer short-wavelength components due to the spatial filtering effect of $1/\cosh(kh_0)$, the total displaced volume at the sea surface is identical to the total volume provided at the sea bottom. This is because the theory assumes the seawater to be an incompressible

fluid (no dilatation), which preserves the total volume of the medium. The total displaced water volume is a conserved quantity for tsunami generation and propagation. This volume can be a good measure for representing the magnitude of a tsunami (e.g., Satake and Kanamori 1991). We should also note that during the propagation, there is the energy conservation by the continuity equation of energy in 2-D form (3.2.3: *Energy Density and Energy Flux Density for Incompressible Fluid*).

5.3.2.5 Initial Velocity Distribution

Equations (5.46) and (5.47) indicate that the velocity distribution has a term including the delta function when the generation process is considered. On the other hand, when the generation process is neglected and only the propagation process is considered, the velocity distribution does not have the term including the delta function (Eqs. (5.51) and (5.52)). These delta-function terms originate from the delta function in the velocity potential (Eq. (5.45)), which represents the sea-bottom deformation as the source. Figure 5.11 shows the amplitudes of the horizontal components of the source terms (proportional to $|\sinh(kz)|$, see Eq. (5.46)) and the vertical component (proportional to $|\cosh(kz)|$, see Eq. (5.47)) for the values of λ=20 and 60 km, normalized by the vertical component at the sea bottom (proportional to $|\cosh(kh_0)|$, see Eq. (5.47)). The vertical component (solid line) decreases from the sea bottom to the sea surface. The horizontal component (dashed line) decreases more rapidly than the vertical component and become almost zero at the sea surface. These are the velocity distributions appearing only during the source process time (see also figures a, b, and c in Figs. 5.6 and 5.7). These terms become zero in the propagation process.

The first term including the step function $H(t)$ in Eqs. (5.46) and (5.47) represents the propagation, but the second term of the delta function $\delta(t)$ does not contribute to the propagation. This indicates that the velocity field caused by the sea-bottom deformation results in the initial tsunami height distribution but does not directly contribute to the propagation. This may defy an intuitive sense that we should set the initial horizontal velocity in the tsunami propagation simulation according to the horizontal velocity distribution caused by the sea-bottom deformation. The analytical solutions of the incompressible fluid theory suggest that we need to set the initial tsunami height distribution as

$$\eta(x,y,0) = \frac{1}{(2\pi)^2}\int_{-\infty}^{\infty}\int_{-\infty}^{\infty} dk_x dk_y\, e^{i(k_x x + k_y y)}\,\frac{\widehat{d}(k_x,k_y)}{\cosh(kh_0)},$$

and we need to set the initial velocity distribution to zero:

$$v_z(x,y,z,0) = 0, \text{and } \mathbf{v_H}(x,y,z,0) = 0$$

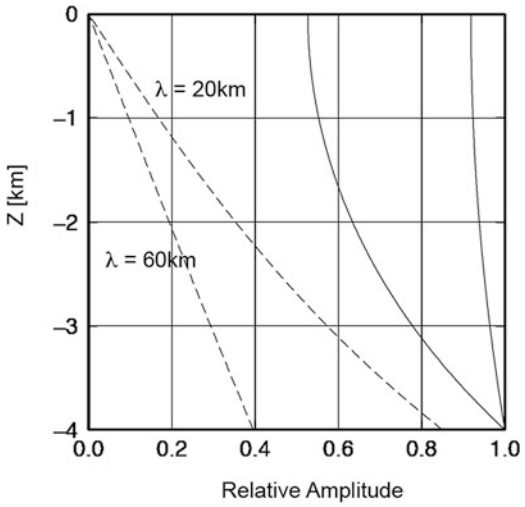

Fig. 5.11 Amplitude of the source term in the horizontal component (dashed lines) and the vertical component (solid lines) normalized by the vertical component at the sea bottom. The cases of $\lambda = 20$ and 60 km (which correspond to $k = 0.3$ and 0.1 km^{-1} when the sea depth is set at 4 km) are plotted (Saito 2013, copyright by Springer)

in tsunami propagation simulations in order to calculate the tsunami η and velocity v_z and $\mathbf{v_H}$ outside the source duration (see Saito 2013). This procedure is the same as that usually used in past studies involving 2-D tsunami simulations (e.g., Fujii and Satake 2008; Saito and Furumura 2009) where the initial velocity distribution is set at zero in the whole space. Equations (5.46) and (5.47) are fundamental equations indicating that we need to make the initial velocity distribution zero but set only the initial tsunami height distribution for the propagation process. These are derived based on a constant sea-depth model. When the sea bottom is not flat, Tanioka and Satake (1996) developed a method to include the horizontal "displacement" into the initial tsunami height distribution. We explain this in Sect. 5.4*: Bridging Generation to Propagation*. On one hand, Song et al. (2017) took the horizontal "velocity" also into account as the initial condition for tsunami simulations. However, the numerical simulations including earthquake faulting, tsunami generation, and propagation suggest that the contribution of the horizontal velocity is negligible in the initial condition for the tsunami simulations (Lotto et al. 2017).

5.3.2.6 Propagation

A comparison of Eqs. (5.46) and (5.51) indicates that they share the distribution function of the horizontal velocity $f_H(k, z, h_0)$ (Eq. (5.58)). The function, hence, is peculiar to the propagation process. The same is true for the function of the vertical velocity $f_z(k, z, h_0)$ (Eq. (5.59)). The functions are

$$f_H(k, z, h_0) \equiv \frac{\cosh[k(z + h_0)]}{\sinh(kh_0)}, \tag{5.58}$$

and

$$f_z(k, z, h_0) \equiv \frac{\sinh[k(z + h_0)]}{\sinh(kh_0)}. \tag{5.59}$$

These indicate the velocity distributions for the horizontal and vertical components, respectively, at a depth z in a sea layer of a constant depth h_0. The same functions are also derived in Eqs. (3.50) and (3.52) for the tsunami propagation process in Chap. 3*: Propagation of Tsunami and Seismic Waves*. The propagation process is typically classified into short-wavelength waves (surface- or deep-water waves) or long-wavelength waves (shallow-water waves) in hydrodynamics (e.g., Gill 1982; Kambe 2007). Figure 5.12a shows the distribution function of the horizontal velocity $f_H(k, z, h_0)$ for values of k = 6.3, 16, 0.1 km^{-1}. These values correspond to the wavelengths of 1, 4, and 60 km for a water depth of 4 km. When the wavelength is λ = 1 km (short-wavelength waves), the horizontal component of the velocity is distributed only in the shallower regions ($z < 1$ km). As the wavelength increases, the distribution function extends deeper. When the wavelength is λ = 60 km (long-wavelength waves), much greater than the water depth h_0 of 4 km, the horizontal velocity component shows a large value (2.3~2.5) over the entire depth, suggesting that horizontal flow occurs in the entire seawater layer. Figure 5.12b shows the distribution function of the vertical velocity $f_z(k, z, h_0)$. Similar to the case of the horizontal component, when the wavelength is $\lambda = 1$ km, the vertical component of the velocity is distributed only in the shallower region ($z < 1$ km). Unlike in the case of the horizontal components, when the wavelength is $\lambda = 60$ km, much greater than the water depth, the vertical component of the velocity decreases with increasing depth and becomes zero at the sea bottom.

5.3.3 Pressure Change

We investigate the pressure change at the sea bottom during tsunami generation based on incompressible fluid theory. It should be noted that assuming a compressible sea is more realistic than assuming an incompressible sea (e.g., Nosov 1999). The seawater compressibility mainly affects the excitation of ocean acoustic waves in high-frequency pressure change ($f > c_0/(4h_0)$) where h_0 is the sea depth and c_0 is the ocean acoustic wave phase velocity (see 3.3.2 *Ocean Acoustic Waves*). The compressibility can also affect longer-period wavefield $f \ll c_0/(4h_0)$, but the effect is minor (e.g., Yamamoto 1982). Therefore, the tsunami generation theory that assumes incompressible fluid provides us with a fundamental concept in tsunami

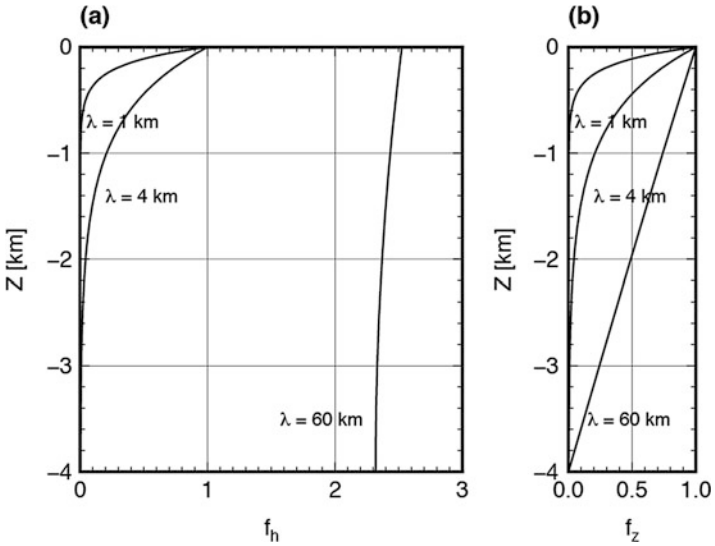

Fig. 5.12 Velocity distribution functions of (**a**) the horizontal component of the velocity (Eq. (5.38)) and (**b**) the vertical component of the velocity (Eq. (5.40)), plotted as functions of the depth, z, with a water depth of $h_0 = 4$ km. The distribution functions for $\lambda = 1$, 4, and 60 km (corresponding to $k = 6.28$, 1.57, and 0.1 km^{-1}, respectively) are plotted

generation. Here, we consider the ocean-bottom pressure change based on the incompressible fluid theory. This is a good approximation for longer-period wavefield $f \ll c_0/(4h_0)$.

Considering the load due to the sea-surface height $\eta(x, y, t)$ on the sea bottom, most past tsunami studies employed a simple relation in the analysis of the ocean-bottom pressure change p_e at the sea bottom $z = -h$ as

$$p_e(x, y, z = -h, t) \approx \rho_0 g_0 \eta(x, y, t), \tag{5.60}$$

where ρ_0 is the seawater density and η is the sea-surface height change. This relation works reasonably when the ocean-bottom pressure gauges are located far from the source region. However, when the ocean-bottom pressure gauges are located inside the source region or near the earthquake hypocenter, this relation is too simple to represent the relation between the pressure change p_e and the sea-surface height η. We need to consider two additional effects in practice.

5.3.3.1 Permanent Sea-Bottom Deformation

As shown in Fig. 5.13, inside the source region, the vertical displacement permanently remains on the sea bottom. The hydrostatic relation (Eq. (3.31)) gives the pressure change Δp as

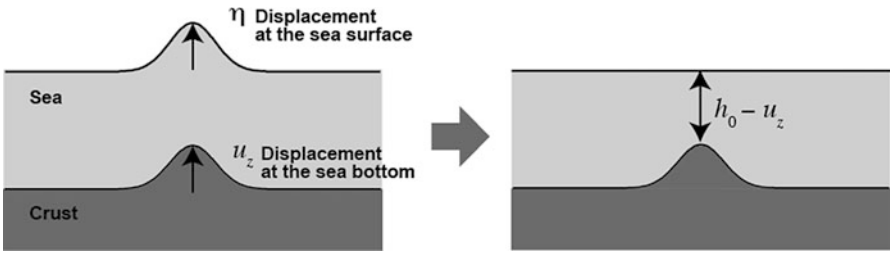

Fig. 5.13 A schematic illustration of the sea-surface displacement η and the sea bottom displacement u_z. (Left) The total sea-depth change caused by the sea-surface and the sea-bottom displacement is $\eta - u_z$. (Right) When the time elapses, the sea-surface displacement η becomes zero. Then the sea depth h_0 changes to $h_0 - u_z$

$$\Delta p(x, y, z) = -\rho_0 g_0 \Delta z. \tag{5.61}$$

When an observation point at the sea bottom uplifts by $u_z(x, y, z = -h, t)$, the station location changes from $(x, y, -h)$ to $(x, y, -h + u_z)$. Then, the pressure at the sea bottom changes by $\Delta p = -\rho_0 g_0 u_z(x, y, z = -h, t)$. Considering this effect in Eq. (5.60), the pressure change is given by

$$p_e(x, y, z = -h, t) = \rho_0 g_0 [\eta(x, y, t) - u_z(x, y, z = -h, t)]. \tag{5.62}$$

Note that the value of $\eta(x, y, t) - u_z(x, y, -h, t)$ is the net sea-depth change at (x, y).

Consider a case in which the sea-bottom deformation occurs instantaneously; in other words, the rate function $\chi(t)$ is given by the delta function as $\chi(t) = \delta(t)$. At the time just after the sea-bottom deformation ends, the tsunami height η is almost the same as the sea-bottom displacement: $\eta(x, y, t \to 0) \approx u_z(x, y, z = -h, t \to 0)$. The slight difference between $\eta(x, y, t \to 0)$ and $u_z(x, y, z = -h, t \to 0)$ is due to a finite sea-depth effect (Fig. 5.9). On the other hand, when we consider that enough time elapses, $t \to \infty$, the sea-surface height or tsunami disappears, $\eta(x, y, t \to \infty) = 0$ (Fig. 5.13). Hence, Eq. (5.62) predicts that the pressure change at the sea bottom behaves as follows:

$$p_e(x, y, z = -h, t) = \begin{cases} 0 & t \to 0 \\ -\rho_0 g_0 u_z(x, y, z = -h, t) & t \to \infty. \end{cases} \tag{5.63}$$

Figure 5.14 shows the observed ocean-bottom pressure records of the 2003 Tokachi-Oki earthquake. In the records of PG1 and PG2, which were located inside the focal area, we recognize that the pressure change behaves as predicted by Eq. (5.63): the pressure change when the earthquake occurred (indicated by vertical dashed lines) was minor, and an offset appeared when ~40 min elapsed.

If we look carefully around the time of the generation at station PG1, we also find high-frequency pressure fluctuation. This pressure fluctuation is caused by another

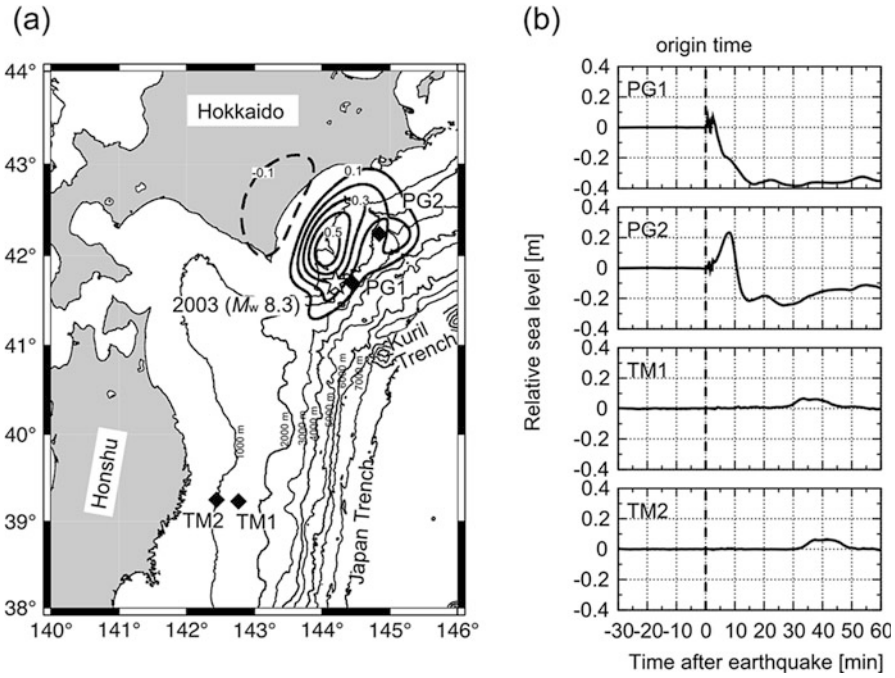

Fig. 5.14 (**a**) Locations of stations of ocean-bottom pressure records PG1, PG2, TM1, and TM2 (black diamonds) and the source region of the 2003 Tokachi-Oki earthquake (black contours). Solid contours show uplift, and dashed contours show subsidence. The contour interval is 0.1 m. The epicenter is indicated by a star. (**b**) Ocean-bottom pressure records. The ocean tide was removed, and a low-pass filter with a cutoff period of 60 s was applied (Tsushima et al. 2012, copyright by the American Geophysical Union)

mechanism. This record shows that the pressure fluctuation is small compared to the pressure changes caused by tsunami and permanent sea-bottom deformation. However, note that the theory described below predicts that this kind of pressure change can be more significant depending on the earthquake rupture.

5.3.3.2 Dynamic Pressure Change

The solution of Eq. (5.49) predicts that the motion of the fluid excites a pressure change. When the vertical velocity at the sea bottom is represented by the Fourier transform as

$$v_z(x,y,z=-h_0,t) = d(x,y)\chi(t) = \frac{1}{(2\pi)^2}\int\int_{-\infty}^{\infty} dk_x dk_y\, e^{i\left(k_x x+k_y y\right)}\widehat{d}\left(k_x,k_y\right)\chi(t), \tag{5.64}$$

the sea-bottom pressure change is then rewritten as

$$\begin{aligned} &p_e(\mathbf{x},t)|_{z=-h_0} \\ &= \frac{1}{(2\pi)^2}\int_{-\infty}^{\infty}\int_{-\infty}^{\infty} dk_x dk_y\, e^{i\left(k_x x+k_y y\right)}\frac{\rho_0\widehat{d}\left(k_x,k_y\right)}{\cosh(kh_0)} \\ &\quad\left\{\frac{g_0}{\cosh(kh_0)}\int_{-\infty}^{t}\cos\left(\omega_0(t-\tau)\right)\chi(\tau)d\tau+\frac{1}{k}\sinh(kh_0)\cdot\int_{-\infty}^{\infty}\frac{d\delta(t-\tau)}{d(t-\tau)}\chi(\tau)d\tau\right\}. \end{aligned}$$

The integration of the second term on the right-hand side is calculated by partial integration, and we obtain

$$\begin{aligned} &p_e(\mathbf{x},t)|_{z=-h_0} \\ &= \frac{1}{(2\pi)^2}\int_{-\infty}^{\infty}\int_{-\infty}^{\infty} dk_x dk_y\, e^{i\left(k_x x+k_y y\right)}\frac{\rho_0\widehat{d}\left(k_x,k_y\right)}{\cosh(kh_0)} \\ &\quad\left\{\frac{g_0}{\cosh(kh_0)}\int_{-\infty}^{t}\cos\left(\omega_0(t-\tau)\right)\chi(\tau)d\tau+\frac{1}{k}\sinh(kh_0)\cdot\frac{d\chi(t)}{dt}\right\} \\ &= \frac{1}{(2\pi)^2}\int_{-\infty}^{\infty}\int_{-\infty}^{\infty} dk_x dk_y\, e^{i\left(k_x x+k_y y\right)} \\ &\quad\left\{\frac{\rho_0 g_0\widehat{\eta}\left(k_x,k_y,t\right)}{\cosh(kh_0)}+\rho_0 h_0\frac{\tanh kh_0}{kh_0}\widehat{a}_z^{bot}\left(k_x,k_y,t\right)\right\}, \end{aligned} \tag{5.65}$$

where $\widehat{\eta}\left(k_x,k_y,t\right)$ is the 2-D spatial Fourier transform of the tsunami height $\eta(x,y,t)$ as

$$\widehat{\eta}\left(k_x,k_y,t\right) = \int\int_{-\infty}^{\infty} dk_x dk_y\, e^{-i\left(k_x x+k_y y\right)}\eta(x,y,t), \tag{5.66}$$

and $\widehat{a}_z^{bot}\left(k_x,k_y,t\right)$ is the 2-D spatial Fourier transform of the vertical acceleration at the sea bottom $a_z^{bot}(x,y,t)$ (see Eq. (5.64)):

$$\begin{aligned} \widehat{a}_z^{bot}\left(k_x,k_y,t\right) &= \int\int_{-\infty}^{\infty} dk_x dk_y\, e^{-i\left(k_x x+k_y y\right)}a_z^{bot}(x,y,t) \\ &= \widehat{d}\left(k_x,k_y\right)\frac{d\chi(t)}{dt}. \end{aligned} \tag{5.67}$$

In particular, when the tsunami wavelength or the wavelength of the sea-bottom deformation is much greater than the sea depth $kh_0 \ll 1$, Eq. (5.65) is approximated to

$$p_e(\mathbf{x},t)|_{z=-h_0} \approx \rho_0 g_0 \eta(x,y,t) + \rho_0 h_0 a_z^{bot}(x,y,t) \quad \text{for } kh_0 \ll 1. \tag{5.68}$$

Equations (5.65) and (5.68) indicate that the sea-bottom pressure change is caused not only by the static loading caused by the tsunami height $\eta(x,y,t)$ (the first term of Eq. (5.65) or (5.68)) but also by the contribution of the acceleration at the sea bottom (the second term of Eq. (5.65) or (5.68)). Since the second term is given by the acceleration or motion of the sea bottom, we referred to this pressure change as the dynamic pressure change. Results of numerical simulations also indicated that the pressure change was caused not only by static pressure change but also by dynamic pressure change (e.g., Kakinuma and Akiyama 2007).

Note that the dynamic pressure is independent of gravity but is excited by the motion of the sea and the crust. In the term $\rho_0 h_0 a_z^{bot}(x,y,t)$, the value of $\rho_0 h_0$ is the mass of the water column per unit area (Fig. 5.15). Therefore, $\rho_0 h_0 a_z^{bot}(x,y,t)$ is the action-reaction force generated when the sea bottom is uplifted with the acceleration $a_z^{bot}(x,y,t)$. Basically, this originates from the inertia of the water column motion (Filloux 1982). The factor of $\tanh kh_0/kh_0$ in Eq. (5.65) indicates the effect of the finite size of the sea-bottom displacement wavelength relative k to the sea depth h_0.

Taking the pressure changes due to the permanent sea-bottom displacement (i) into account in Eq. (5.65), we represent the sea-bottom pressure change caused by the sea-bottom deformation $u_z(x,y,-h,t)$ as

$$\begin{aligned} & p_e(\mathbf{x},t)|_{z=-h_0} \\ & = \frac{1}{(2\pi)^2}\int_{-\infty}^{\infty}\int_{-\infty}^{\infty} dk_x dk_y\, e^{i(k_x x + k_y y)} \\ & \qquad \left\{ \frac{\rho_0 g_0 \widehat{\eta}(k_x,k_y,t)}{\cosh(kh_0)} + \rho_0 h_0 \frac{\tanh kh_0}{kh_0} \widehat{a}_z^{bot}(k_x,k_y,t) \right\} \\ & \quad - \rho_0 g_0 u_z(x,y,z=-h,t) \\ & \approx \rho_0 g_0 \{\eta(x,y,t) - u_z(x,y,-h)\} + \rho_0 h_0 a_z^{bot}(x,y,t) \quad \text{for } kh_0 \ll 1. \end{aligned} \tag{5.69}$$

Figure 5.16 shows an example of the actual observed ocean-bottom pressure record (Kubota et al. 2015). A low-pass filter of 100 s was applied to the ocean-bottom pressure records. This record clearly indicates a large dynamic pressure

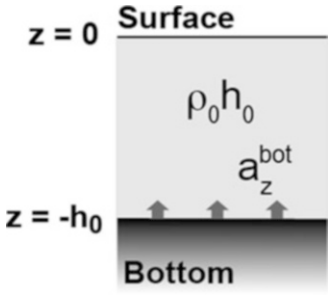

Fig. 5.15 The mass of the water column is $\rho_0 h_0$ per unit area where ρ_0 is the water density and h_0 is the water column height. The vertical acceleration at the bottom is $a_z^{bot}(x,y,t)$

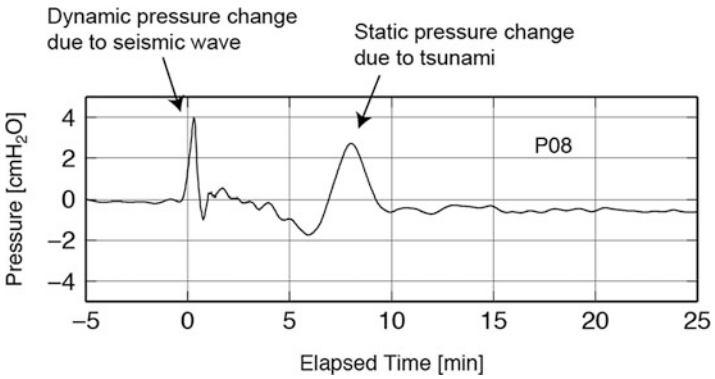

Fig. 5.16 Ocean-bottom pressure record observed at the gauge located ~50 km away from the hypocenter of a moderate-size earthquake (M_W 7.0) that occurred on July 10, 2011, offshore from the coast of northeastern Honshu, Japan. The pressure change of 1 cmH_2O corresponds to the hydrostatic pressure due to a water depth of 1 cm (1 $cmH_2O = 98$ Pa) (Kubota et al. 2015 Copyright by the American Geophysical Union)

change caused by seismic waves in addition to the static pressure change caused by the tsunami. The dynamic pressure change may function as significant noise when analyzing the pressure records within a short elapsed time (a few minutes after the earthquake occurs). On the other hand, because the dynamic pressure change represents the sea-bottom acceleration, we expect that the dynamic component in the ocean-bottom pressure records can be used for the estimation of the kinematic parameters of the earthquake fault motion (e.g., rise time and source time duration). Investigating how to use the dynamic component as seismic signals would be an interesting challenge (e.g., An et al. 2017; Kubota et al. 2017).

5.3.3.3 Comparison with Elastic Dynamic Theory

The incompressible fluid theory has been employed without considering seawater elasticity. It would be important to validate whether the dynamic pressure change appears in the seismic wave simulations. Supposing a 2-D space composed of an elastic water layer and an elastic crust (Fig. 5.17a), the sea-bottom pressure change caused by earthquake fault motion was simulated. The gray line in Fig. 5.17b (under the blue and red lines) shows the temporal variation of the sea-bottom pressure change p_e inside the focal area when the earthquake fault has a fault width $W = 100$ km and a rupture duration of $t_c = 40$ s (the station location is indicated by a triangle in Fig. 5.17a). The dynamic pressure change begins to increase at 40 s and takes a maximum value of 0.008 MPa at the elapsed time of 55 s. The blue line indicates the temporal change of the sea-bottom acceleration $a_z^{bot}(x, y, t)$; here the dimension is converted to pressure according to $\rho_0 h_0 a_z^{bot}(x, y, t)$. The red line

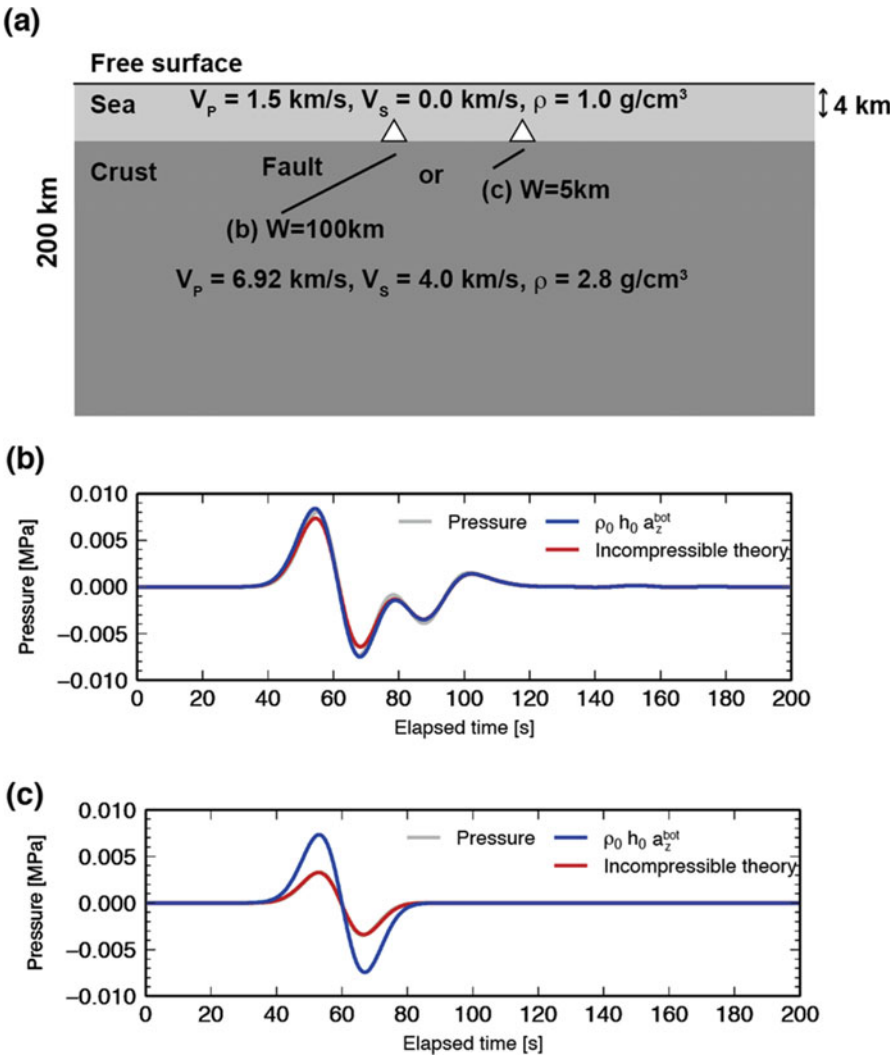

Fig. 5.17 (**a**) A schematic illustration of the simulation settings. Elastic medium consisting of a water layer and homogeneous crust. The finite size of the earthquake fault is set in the crust. A large earthquake (fault width of $W = 100$ km) and small earthquake ($W = 5$ km) are supposed. Locations of hypothesized stations are plotted by triangles. (**b**) Sea-bottom pressure change (gray) on the sea bottom inside the source region for the large earthquake ($W = 100$ km). The pressure change predicted by a simple relation $\rho_0 h_0 a_z^{bot}$ (blue) and Eq. (5.65) assuming the incompressible fluid theory (red) where a_z^{bot} is the acceleration on the sea bottom. (**c**) Same as (b) but for the small earthquake ($W = 5$ km). The red line and gray line (under the red line) are almost identical (Saito 2017 copyright by Oxford Academic)

indicates the temporal change of the sea-bottom acceleration $a_z^{bot}(x, y, t)$ where the dimension is converted to pressure using a spatial low-pass filter of $\rho_0 h_0 \tanh kh_0/kh_0$ (see Eq. (5.65)). Excellent agreement among the three lines was confirmed for the case of $W = 100$ km.

A comparison is also shown for the case when the earthquake fault width is short ($W = 5$ km) in Fig. 5.17c. We found that the simple theoretical relation $\rho_0 h_0 a_z^{bot}$ (blue) does not agree with the sea-bottom pressure change (gray, but this is not visible in the figure because the gray line is under the red line), while the pressure change obtained by applying the spatial low-pass filter of $\rho_0 h_0 \tanh kh_0/kh_0$ to the sea-bottom acceleration a_z^{bot} (red) shows good agreement with the sea-bottom pressure change (gray). The prediction based on the incompressible fluid theory can be confirmed in the elastic dynamic simulation. This supports the validity of the incompressible fluid theory.

5.3.3.4 Dynamic Pressure Change and Static Pressure Change

When using ocean-bottom pressure gauges deployed inside the focal area, even after removing the ocean acoustic waves with an appropriate low-pass filter, the pressure records still include the contribution of the dynamic pressure change caused by the sea-bottom acceleration. Figure 5.18 shows an example of a synthesized ocean-bottom pressure record inside the focal area. The red line shows the pressure change including both the dynamic and static contributions, whereas the bold gray line shows the pressure change including only the static contribution. The static pressure change (bold gray line) is zero at the elapsed time of zero because the vertical displacements at the sea surface and sea bottom are almost the same. When enough time elapses, the pressure change shows an offset value of -10 mH_2O. This is because the sea bottom is uplifted by 10 m. On the other hand, if we observe the pressure change including the dynamic contribution (red line), it shows a large impulsive signal at the elapsed time of 80 s. This does not reflect the sea-surface height change, but this large impulsive signal is excited by the dynamic pressure change. We should take care not to consider this pressure change to be the sea-surface height change just by using a simple hydrostatic relation $p_e = \rho_0 g_0 \eta$. The dynamic pressure change was actually observed by the ocean-bottom pressure gauge deployed in deep ocean (see Fig. 5.16). If this dynamic pressure change is mistakenly considered to be the tsunami height in real-time tsunami monitoring, it may cause incorrect tsunami prediction at the coast. It would be challenging to develop a method to distinguish the dynamic pressure change (seismic waves) and the static pressure change (tsunami) in real time.

We examine the contribution to the dynamic pressure change made by the sea-bottom acceleration $\rho_0 h_0 a_z^{bot} = \rho_0 h_0 \ddot{u}_z$ (u_z is the vertical displacement at the sea bottom) relative to the hydrostatic pressure change caused by the sea-surface

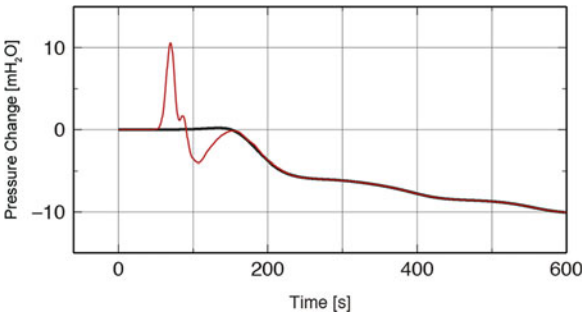

Fig. 5.18 Synthesized ocean-bottom pressure gauge records. Ocean-bottom pressure change with the dynamic pressure change (red) and without the dynamic pressure change (black). A pressure change of 1 mH_2O corresponds to the hydrostatic pressure due to a water depth of 1 m ($1mH_2O = 9.8$ MPa) (Saito and Tsushima 2016, copyright by the American Geophysical Union)

height $\rho_0 g_0 \eta(x, y, t)$. The ratio of the dynamic pressure change to the static pressure change is given by

$$R_D = \frac{h_0 |\ddot{u}_z|}{g_0 |\eta|}. \tag{5.70}$$

If the dominant angular frequency of the vertical displacement at the bottom is ω_c, the acceleration is given by $|\ddot{u}_z| = \omega_C^2 |u_z|$. The sea-surface height is approximately $|\eta| \sim |u_z|$. The ratio is approximately given by

$$R_D \sim \frac{h_0 \omega_C^2 |u_z|}{g_0 |u_z|} = \frac{h_0 \omega_c^2}{g_0}. \tag{5.71}$$

The duration of the sea-bottom deformation t_c is approximately half of the dominant period $t_c \sim \pi/\omega_c$. The ratio is then

$$R_D \sim \frac{\pi^2 h_0}{g_0 t_c^2} \sim \frac{10 h_0}{g_0 t_c^2}. \tag{5.72}$$

This indicates that the contribution of the dynamic pressure change is basically controlled by the duration of the sea-bottom deformation (or this corresponds to the rise time) t_c and decreases rapidly with increasing duration. For example, we consider $R_D = 1/2$ to be a condition that the dynamic pressure change significantly contaminates the static pressure change. The duration t_c is about 90 s if we suppose $h_0 = 4000$ m as an average ocean depth. This indicates that it is inappropriate to assume hydrostatic approximation during ~90 s from the time the sea bottom begins to rise.

5.4 Bridging Generation to Propagation

Sections 5.1, 5.2, and 5.3 have investigated the fundamental mechanism of tsunami generation by supposing a flat sea bottom. It is important to consider the effects of bathymetry when analyzing or simulating realistic records. This section bridges the gap between the analytical solutions derived under a constant sea-depth assumption and tsunami simulations with realistic bathymetry.

5.4.1 Contribution of Sea-Depth Variation

When the flat sea bottom is assumed, the horizontal displacement is allowed to be discontinuous at the boundary between the fluid and solid. Only the vertical component of the displacement should be continuous at the boundary between the fluid and solid (e.g., Ewing et al. 1957; Kennett 2001). Hence, the horizontal displacement at the sea bottom does not excite vertical flow in the sea (note that the vertical displacement at the sea bottom excites horizontal flow in the sea layer during the generation. See Fig. 5.11). When the sea bottom is not flat but is curved, the combination of the horizontal displacement and the sea-bottom topography can excite vertical flow (e.g., Nosov and Kolesov 2011). This mechanism was first taken into account in setting the initial tsunami height distribution by Tanioka and Satake (1996). After the 2011 Tohoku-Oki earthquake, which showed a large horizontal displacement near a deep trench (e.g., Ito et al. 2011), numerous studies pointed out the contribution of the horizontal displacement to the tsunami excitation (e.g., Gusman et al. 2012; Satake et al. 2013; Hooper et al. 2013). Here we introduce the contribution of the sea-bottom horizontal displacement to the tsunami generation process.

Consider the case where the sea bottom is not flat as shown in Fig. 5.19. The displacement normal to the boundary between the sea and crust is continuous at the boundary, whereas the tangential components of the displacement can be discontinuous. When the sea bottom (or top of the crust) is displaced by the displacement vector $\mathbf{u}$, the normal component u_n is continuous on the boundary between the fluid and solid.

The unit vector $\bar{\mathbf{n}}$ normal to the sea bottom $z = -h(x, y)$ is given by

$$\bar{\mathbf{n}} = \frac{1}{\sqrt{(\partial h/\partial x)^2 + (\partial h/\partial y)^2 + 1}} \left(\frac{\partial}{\partial x} h(x, y), \frac{\partial}{\partial y} h(x, y), 1 \right). \tag{5.73}$$

Consider the displacement vector at the top of the crust, $\mathbf{u}(x, y, -h - 0)$. The component of the displacement vector normal to the sea bottom is then given by

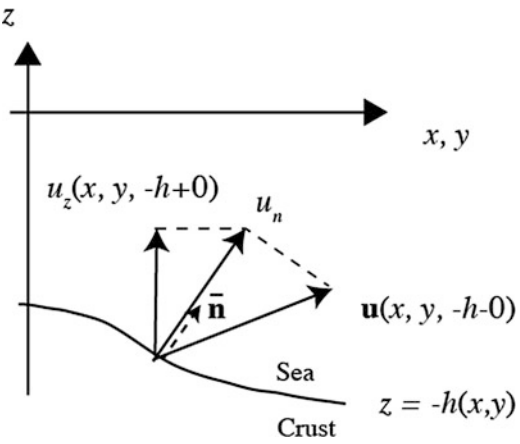

Fig. 5.19 The sea depth is given as a function of the horizontal coordinates (x, y), $z = -h(x, y)$. The bottom of the sea is just above the boundary between the sea and crust, $z = -h(x, y) + 0$, while the top of the crust is just below the boundary $z = -h(x, y) - 0$. The displacement vector at the top of crust is $\mathbf{u} = \mathbf{u}(x, y, -h - 0)$. The bathymetry curve is characterized by the normal vector $\bar{\mathbf{n}}$. The displacement normal to the bathymetry is given by $u_n = \mathbf{u} \cdot \bar{\mathbf{n}}$, which is continuous between the crust and sea. The vertical component at the bottom of the sea is $u_z(x, y, -h + 0)$

$$u_n = \mathbf{u} \cdot \bar{\mathbf{n}} = \frac{1}{\sqrt{(\partial h/\partial x)^2 + (\partial h/\partial y)^2 + 1}} \left(u_x \frac{\partial h}{\partial x} + u_y \frac{\partial h}{\partial y} + u_z \right) \Big|_{z=-h-0}. \quad (5.74)$$

Since the normal component is continuous between the boundary, $u_n(x, y, -h + 0) = u_n(x, y, -h - 0)$, the displacement vector at the bottom of the sea is given by

$$\mathbf{u}(x, y, -h + 0) = u_n(x, y, -h - 0)\bar{\mathbf{n}}. \quad (5.75)$$

The vertical component of the sea-bottom displacement $\mathbf{u}(x, y, -h + 0)$ would contribute to the vertical displacement at the sea surface. The projection of the displacement vector $\mathbf{u}(x, y, -h + 0)$ to the vertical axis gives the vertical component at the sea bottom as

$$\begin{aligned} u_z(x, y, -h + 0) &= \mathbf{u}(x, y, -h + 0) \cdot \mathbf{e_z} \\ &= u_n \bar{\mathbf{n}} \cdot \mathbf{e_z} \\ &= \frac{1}{(\partial h/\partial x)^2 + (\partial h/\partial y)^2 + 1} \left(u_x \frac{\partial h}{\partial x} + u_y \frac{\partial h}{\partial y} + u_z \right) \Big|_{z=-h-0}. \end{aligned} \quad (5.76)$$

Equation (5.76) represents the vertical displacement at the bottom of the sea $u_z(x, y, -h + 0)$ by using the displacement at the top of the crust $(u_x, u_y, u_z)|_{z=-h-0}$ and the sea depth $z = -h(x, y)$. When the sea depth varies smooth enough as

$$\left(\frac{\partial h}{\partial x}\right)^2 + \left(\frac{\partial h}{\partial y}\right)^2 \ll 1, \tag{5.77}$$

the vertical displacement at the bottom of the water layer is approximately given by

$$u_z(x, y, -h + 0) \approx \left(u_x \frac{\partial h}{\partial x} + u_y \frac{\partial h}{\partial y} + u_z\right)\Big|_{z=-h-0}. \tag{5.78}$$

We may consider the displacement $(u_x, u_y, u_z)|_{z = -h-0}$ (the right-hand side of Eq. (5.78)) as the displacement vector on the sea bottom. This is often calculated as the sea-bottom displacement with the code of Okada (1985) or other seismic numerical codes. The vertical displacement $u_z(x, y, -h + 0)$ on the left-hand side is an effective vertical component of the displacement vector generating the initial tsunami height distribution. If we convolve $u_z(x, y, -h + 0)$ with Kajiura's equation (Eq. (5.55)), we obtain a reasonable initial tsunami height distribution for the 2-D tsunami propagation simulations. Equation (5.78) is the same as the equation originally proposed by Tanioka and Satake (1996).

Convincing evidence regarding the contribution of the horizontal displacement to the tsunami excitation was observed during the 2011 Tohoku-Oki earthquake. The black lines in Fig. 5.20a, b show the sea-surface height change observed at the two tide gauges during the Tohoku-Oki earthquake. The blue lines show the theoretically calculated sea-surface height that includes only the contribution from the vertical displacement at the sea bottom. These theoretical calculations can reproduce some parts of the observed records. On the other hand, if the horizontal components are taken into account in setting the initial tsunami height distribution, the theoretically calculated sea-surface height change (red line) successfully explains the overall features of these observations. The two stations used in this comparison are located on the western coast of Honshu, Japan (Fig. 5.20c), where a large tsunami coming from the main tsunami source is blocked by the Japanese mainland. Also, as shown in Fig. 5.20c and d, there were large horizontal displacement compared to vertical displacement. These conditions made it possible to observe convincing evidence indicating the contribution of horizontal displacement to the tsunami excitation.

The fault motion of the 2011 Tohoku-Oki earthquake causes a large horizontal displacement around the deep and steep Japan Trench. Equation (5.78) indicates that these two conditions (large horizontal displacement at a large bathymetry gradient) would efficiently cause the initial tsunami height distribution. By considering the horizontal displacement in calculating the initial tsunami height distribution in the simulation, the tsunami simulation predicts a larger tsunami amplitude (Fig. 5.21).

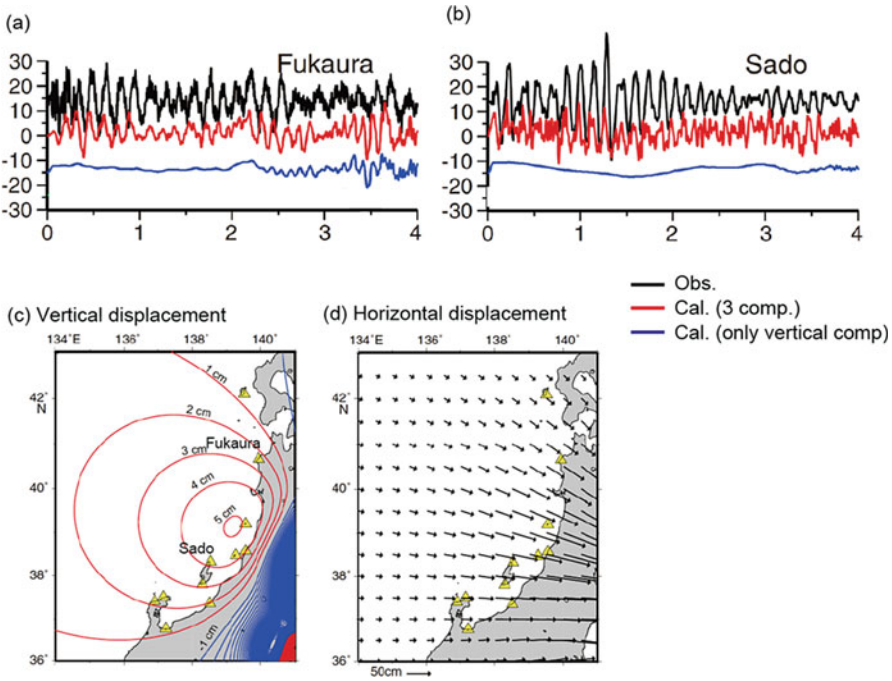

Fig. 5.20 (**a**) Observed and calculated tsunami waveforms at Fukaura (location is plotted in (c)). The black line shows the observed waveform. The red line is the waveform calculated from the total vertical seafloor displacement including the effects of the horizontal displacement. The blue line is the waveform calculated from the vertical displacement. (**b**) Observed and calculated waveforms at Sado. (**c**) Vertical displacement and (**d**) horizontal displacement around Japan calculated from the fault model of the 2011 Tohoku earthquake (Murotani et al. 2015 copyright by Springer)

5.4.2 *Synthesis of Ocean-Bottom Pressure Records*

We often use the terms "tsunami waveforms" and "tsunami data." Some people may assume that the temporal change of sea-surface displacement is a tsunami waveform, and others may suppose that the sea-bottom pressure change is a tsunami waveform. It is important to recognize what sensor is being used when referring to tsunami data or tsunami waveforms. If one uses tide gauges or GPS sensors, the tsunami waveform corresponds to the vertical sea-surface displacement $u_z(x, y, z_{\mathrm{sur}}, t)$ where $z = z_{\mathrm{sur}}$ is the sea surface. If ocean-bottom pressure gauges are used, the tsunami waveform represents the pressure change at the sea bottom $p_e(x, y, z_{\mathrm{bot}}, t)$ where $z = z_{\mathrm{bot}}$ is the sea bottom. In most cases, after an appropriate low-pass filter is applied, the two values are simply related by a hydrostatic approximation as $p_e(x, y, z_{\mathrm{bot}}, t) = \rho_0 g_0 u_z(x, y, z_{\mathrm{sur}}, t)$ where ρ_0 is the seawater density and g_0 is the gravitational acceleration. However, we cannot use this relation when the sensor is located near the focal area where permanent sea-bottom displacement can occur and the seismic

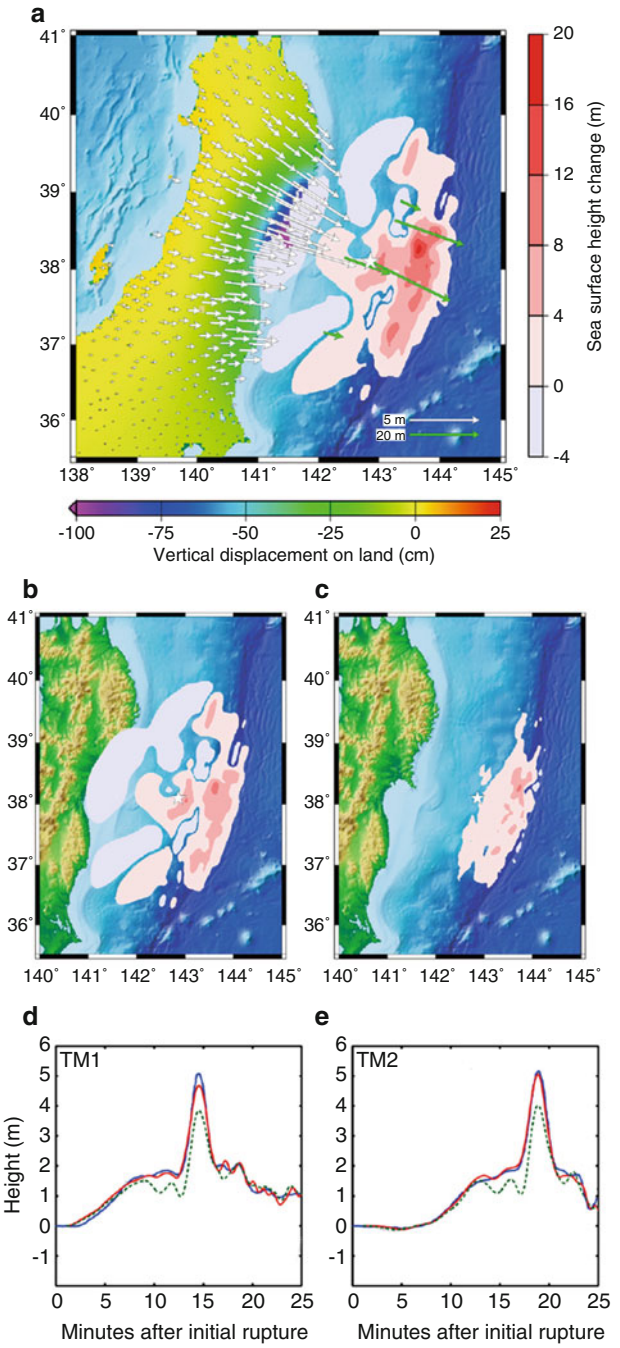

Fig. 5.21 Initial sea-surface height distribution. Red and blue contour colors represent the sea-surface height distribution considering (**a**) the total vertical sea-bottom displacement including both vertical and horizontal displacement, (**b**) the vertical displacement only, and (**c**) the vertical

waves overlap tsunami. This section illustrates a method of synthesizing the ocean-bottom pressure records by taking into account both the seismic waves and tsunami.

There are two methods by which to introduce a source in the tsunami simulations (Fig. 5.22). In Chap. 4, by assuming that the sea layer is compressible ((b) in Fig. 5.22), we synthesized the sea-surface displacement caused by the seismic waves and tsunami. This section synthesizes the ocean-bottom pressure change. We here assume an incompressible sea layer and employ the method shown in (a) in Fig. 5.22. This is because it is reasonable to assume an incompressible sea when calculating the static pressure change.

We propose a two-step method composed of linear and nonlinear simulations (Fig. 5.22a, c). The flowchart is shown in Fig. 5.23. In this method, we decompose the pressure change into two components. One is the pressure change caused by gravity. This contribution is calculated by the tsunami simulation. This corresponds to the static pressure change p_{static}. The other is the pressure change caused by seismic waves, which is excited even when gravity is zero. This is the dynamic pressure change p_{dynamic}. The total pressure change p_{e} is represented as $p_{\mathrm{e}} = p_{\mathrm{dynamic}} + p_{\mathrm{static}}$.

In the first step, we calculate the spatial and temporal distribution of the sea-bottom motion generated by an earthquake. This simulation also calculates the sea-bottom pressure change corresponding to a dynamic pressure change. The particle motion in an elastic medium satisfies the linear equations of motion:

$$\rho \frac{\partial^2 u_i}{\partial t^2} = \tau_{ij,j} + f_i, \tag{5.79}$$

and satisfies a constitutive law,

$$\tau_{ij} = \lambda \delta_{ij} u_{k,k} + \mu \left(u_{i,j} + u_{j,i} \right), \tag{5.80}$$

where τ_{ij} is the stress tensor in the medium. These equations are commonly used in many seismological studies (e.g., Aki and Richards (2002)). The parameters λ and μ are Lamé parameters, which represent the properties of the medium. An equivalent body force of the double couple force system for a point dislocation source is used to represent an earthquake (e.g., Eqs. (4.10) and (4.7) in Chap. 4). We saved the simulation results of the spatial and temporal distribution of the vertical velocity at

Fig. 5.21 (continued) displacement from the horizontal displacement and bathymetry effect. (**d**), (**e**) Tsunami waveforms at two offshore sea-bottom pressure gauges. The blue lines show the observed waveforms. The red lines show the waveforms calculated from the total vertical sea-bottom displacement. The green dashed lines are the waveforms calculated from the vertical displacement (Hooper et al. 2013, copyright by Elsevier)

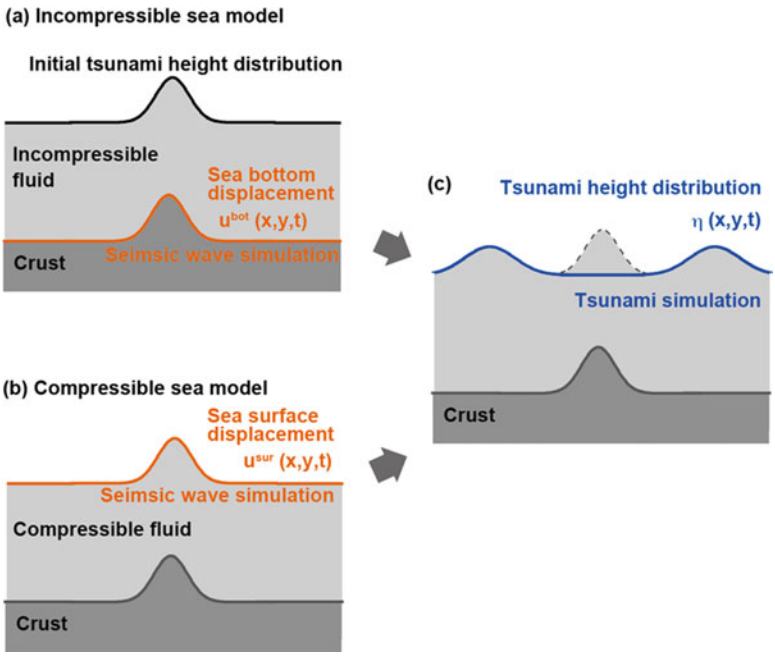

Fig. 5.22 Incompressible sea model and compressible sea model for tsunami simulations. (**a**) The sea is assumed to be an incompressible fluid. (**b**) The sea is assumed to be a compressible fluid. (**c**) Tsunami propagation is calculated based on the tsunami equations in the incompressible sea

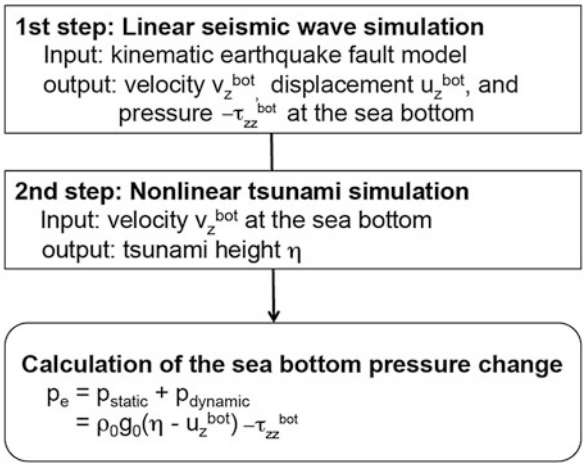

Fig. 5.23 Flowchart of the ocean-bottom pressure record synthesis

the sea bottom v_z^{bot} and used them as a source in the tsunami simulation in the next step. Additionally, we saved the simulated vertical displacement u_z^{bot} and the stress (pressure) τ_{zz}^{bot} at the sea bottom for the later synthesis of the ocean-bottom pressure records.

In the second step, we calculate the tsunami propagation by using the velocity field at the sea bottom v_z^{bot} as a source. According to the incompressible fluid theory, when the vertical displacement at the sea bottom given by $u_z^{\mathrm{bot}}(x,y)$ occurs instantaneously, the sea-surface height is given by Eq. (5.81) exp(..)

$$\eta_0(x,y) = \frac{1}{(2\pi)^2}\int\int_{-\infty}^{\infty} dk_x dk_y \exp\left[i\left(k_x x + k_y y\right)\right] \frac{\tilde{u}_z^{\mathrm{bot}}\left(k_x,k_y\right)}{\cosh(kh_0)}, \tag{5.81}$$

where $\tilde{u}_z^{\mathrm{bot}}\left(k_x,k_y\right)$ is the 2-D Fourier transform of the vertical displacement distribution at the bottom $u_z^{\mathrm{bot}}(x,y)$ (e.g., Kajiura 1963; Saito and Furumura 2009). Note that when we intend to include the horizontal displacement contribution, we should use Eq. (5.78) for $u_z^{\mathrm{bot}}(x,y)$.

Then, the sea-surface elevation during a fractional duration Δt excited by the time-dependent sea-bottom deformation is given by

$$\Delta\eta_0(x,y,t) = \frac{1}{(2\pi)^2}\int\int_{-\infty}^{\infty} dk_x dk_y \exp\left[i\left(k_x x + k_y y\right)\right] \frac{\tilde{v}_z^{\mathrm{bot}}\left(k_x,k_y,t\right)}{\cosh(kh_0)}\Delta t, \tag{5.82}$$

where $\tilde{v}_z^{\mathrm{bot}}\left(k_x,k_y,t\right)$ is the 2-D Fourier transform of the vertical velocity distribution at the bottom $v_z^{\mathrm{bot}}(x,y,t)$. Substituting the vertical velocity at the sea bottom calculated in the first step of the seismic wave simulation into Eq. (5.82), we obtain the tsunami height increment $\Delta\eta_0(x,y,t)$ for the small time interval Δt at the time t.

The tsunami propagation is assumed to be described by the tsunami equations (see Chap. 6: *Propagation Simulation*). The sea-surface elevation in a fractional duration given by Eq. (5.82) is added to the sea-surface height distribution at each time step. The simulated spatial and temporal distribution of the sea-surface height $\eta(x,y,t)$ is saved to synthesize the ocean-bottom pressure records.

Ocean-bottom pressure records are synthesized using the results of these seismic and tsunami simulations. An ocean-bottom pressure change is considered to be composed of static and dynamic components. The static component of the ocean-bottom pressure change caused by gravity is given by

$$p_{\mathrm{static}} = \rho_0 g_0\left(\eta - u_z^{\mathrm{bot}}\right) \tag{5.83}$$

where the sea-surface height displacement $\eta(x,y,t)$ and the vertical sea-bottom displacement $u_z^{\mathrm{bot}}(x,y,t)$ are calculated in the tsunami and seismic simulations, respectively. On the other hand, the dynamic ocean-bottom pressure change is given by

$$p_{\mathrm{dynamic}} = -\tau_{zz}^{\mathrm{bot}}(x,y,t). \tag{5.84}$$

The stress at the bottom τ_{zz}^{bot} is calculated in the seismic wave simulation. Note that the sign of the pressure is opposite to that of the stress, and the stress is isotropic

as $\tau_{xx} = \tau_{yy} = \tau_{zz}$ in the sea layer. The total pressure change at the sea bottom is given by

$$p_e = p_{\text{static}} + p_{\text{dynamic}}. \tag{5.85}$$

5.4.2.1 Synthesized Ocean-Bottom Pressure Waveforms

Figure 5.24a shows the ocean-bottom pressure records observed at a station near the focal area of the 2011 Tohoku-Oki earthquake. The record shows the dominant high-frequency component of the pressure change up to an elapsed time of ~500 s. These are mainly ocean acoustic waves. Applying the low-pass filter with a cutoff frequency of 60 s to the record, we remove the ocean acoustic waves and obtain low-frequency component records (Fig. 5.24b). The ocean-bottom pressure change caused by the tsunami is clearly recognized from the elapsed time of 0–1200 s. Moreover, we recognize that the low-frequency wave also appears at the elapsed time of ~100 s. This is the pressure change caused by low-frequency seismic waves.

Figure 5.24c shows the ocean-bottom pressure change simulated by the method described in this chapter. We used a rectangle fault plane with a length of 200 km and a width of 150 km with a uniform slip of 20 m. The depth of the centroid of the fault is set at a depth of 50.5 km. The strike, dip, and rake are set at 200°, 30°, and 90°, respectively. The slip starts simultaneously on the fault, and the rise time is set at $t_c = 30$ s. The simulated waveform indicates the pressure change due to the seismic wave at around 100 s with an amplitude of ~2 mH_2O, and the pressure gradually increases. The maximum value was ~5 mH_2O at ~900 s. The simulated ocean-bottom pressure record roughly reproduced the observed record, even though a uniform slip and simple source time function were assumed in the simulation.

Figure 5.25 compares the synthesized ocean-bottom pressure change for various simulation settings. The light gray line represents the synthesized pressure change including the ocean acoustic waves, low-frequency seismic waves, and tsunami. The synthesized pressure change contains less high-frequency component than the observed records (e.g., see Fig. 5.24a). This is mainly because the earthquake fault model used in this synthesis was characterized by a smoother slip distribution than the actual earthquake. By applying the low-pass filter to the synthesized pressure change (light gray line) and removing the ocean acoustic waves, we obtain a red line that contains low-frequency seismic waves and tsunami. The dark gray line represents the synthesized pressure change including only the tsunami component, i.e., the static pressure change p_{static} in Eq. (5.85). These comparisons clearly indicate that both high- and low-frequency seismic waves significantly contribute to the ocean-bottom pressure waveforms. Even if the low-pass filter is applied, the low-frequency seismic wave still exists in the waveform. This suggests that low-frequency seismic waves can function as noise when ocean-bottom pressure records are analyzed as

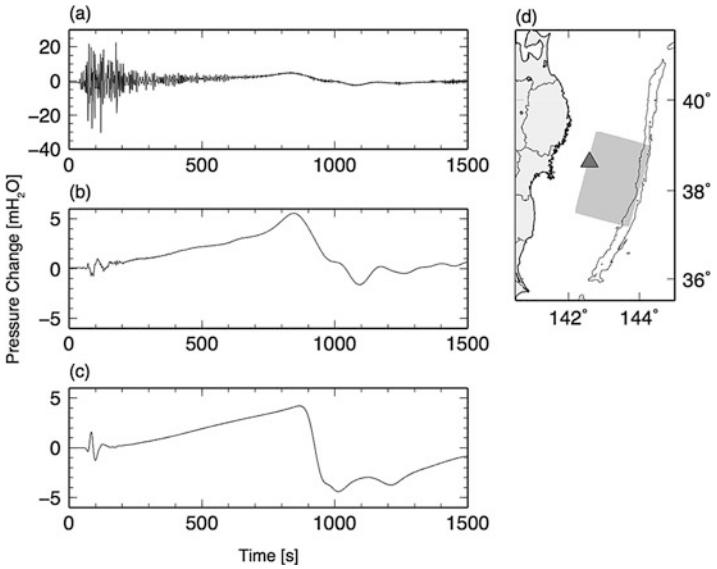

Fig. 5.24 (**a**) Ocean-bottom pressure record of the 2011 Tohoku-Oki earthquake observed at station P06 (a gray triangle in (d)). (**b**) Low-frequency component of the ocean-bottom pressure record obtained by the low-pass filter with a cutoff frequency of 60 s. (**c**) Simulated ocean-bottom pressure change at the station. (**d**) The locations of the station (triangle) and source model of the 2011 Tohoku-Oki earthquake (rectangle) (Saito and Tsushima 2016, copyright by the American Geophysical Union)

tsunami signal. It is important to be especially careful when using ocean-bottom pressure records in an automated tsunami analysis system so as not to mistake low-frequency seismic waves as tsunami.

Appendices

Appendix 5A: Equation (5.28)

We derive Eq. (5.28) from Eq. (5.27). In Eq. (5.27), the residue theorem is used with respect to the integration over the angular frequency. Since the poles are located on the path of integration, we introduce artificial damping parameters to shift the poles from the path and to integrate with the residue theorem. These artificial damping parameters will be taken to be zero after the integration using the residue theorem. An artificial damping parameter ($\varepsilon_1 > 0$) is introduced in Eq. (5.10) as

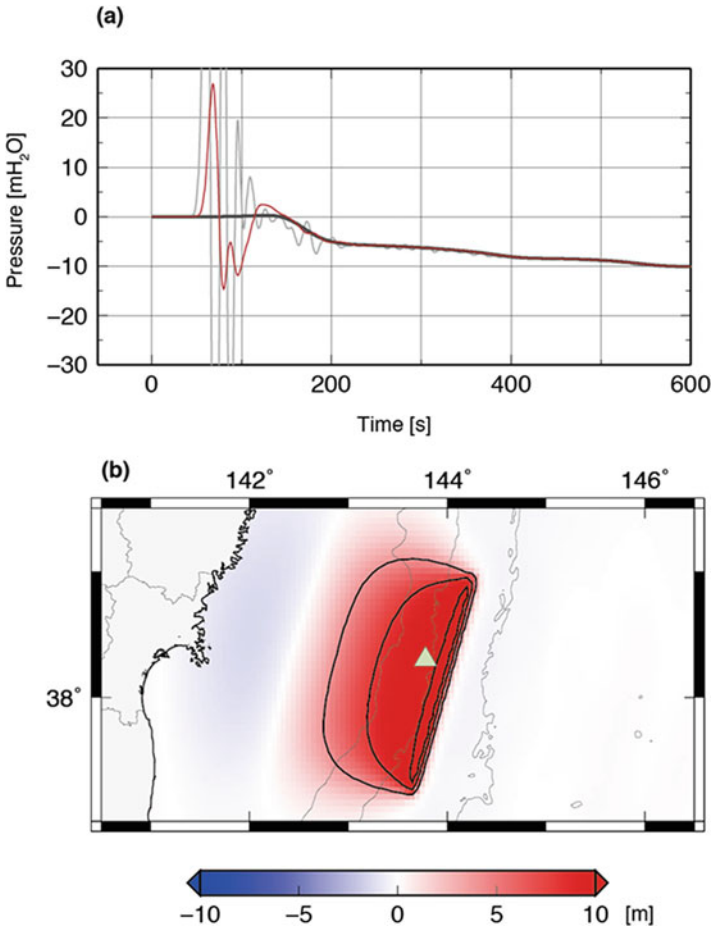

Fig. 5.25 (**a**) Simulated waveforms at a station inside the focal area (the location is indicated in (b)). A synthesized ocean-bottom pressure change including ocean acoustic waves, low-frequency seismic waves, and tsunami (light gray line). The low-pass filter with a cutoff period of 60 s is applied to the simulated waveform (red lines and dark gray lines). The red line is the total pressure change. The dark gray line shows the pressure change due to only the static component. (**b**) The station location and the vertical displacement distribution (Saito and Tsushima 2016, copyright by the American Geophysical Union)

$$\left.\frac{\partial \phi(\mathbf{x},t)}{\partial t}\right|_{z=0} + g_0 \eta(x,y,t) = -2\varepsilon_1 \phi(\mathbf{x},t)|_{z=0}. \tag{5.5A.1}$$

Using another surface boundary condition (Eq. (5.9)):

$$\frac{\partial \eta(x,y,t)}{\partial t} = \left.\frac{\partial \phi(\mathbf{x},t)}{\partial z}\right|_{z=0}, \tag{5.5A.2}$$

and (5.5A.1), we obtain

$$\left.\frac{\partial^2 \phi(\mathbf{x},t)}{\partial t^2}\right|_{z=0} + g_0 \left.\frac{\partial \phi(\mathbf{x},t)}{\partial z}\right|_{z=0} = -2\varepsilon_1 \left.\frac{\partial \phi(\mathbf{x},t)}{\partial t}\right|_{z=0}, \tag{5.5A.3}$$

instead of Eq. (5.11) and

$$\left(\frac{d}{dz} - \frac{\omega^2 + 2i\epsilon_1\omega}{g_0}\right)\widehat{\phi}\left(k_x,k_y,z,\omega\right)\Big|_{z=0} = 0, \tag{5.5A.4}$$

instead of Eq. (5.20).

Additionally, another artificial damping parameter ($\varepsilon_2 > 0$) is introduced in Eq. (5.24) as

$$\chi(t) = \frac{1}{T}[H(t) - H(t-T)]e^{-\varepsilon_2 t}. \tag{5.5A.5}$$

Then, we obtain

$$\widehat{\chi}(\omega) = \int_{-\infty}^{\infty} \chi(t) e^{i\omega t} dt = \frac{1}{i(\omega + i\epsilon_2)T}\left(e^{i(\omega+i\epsilon_2)T} - 1\right). \tag{5.5A.6}$$

When Eqs. (5.5A.4) and (5.5A.6) are used, the equation corresponding to Eq. (5.27) is written as

$$\begin{aligned}
&\phi(x,y,z,t) \\
&= \frac{1}{(2\pi)^2}\int_{-\infty}^{\infty}\int_{-\infty}^{\infty} dk_x dk_y\, e^{i\left(k_x x + k_y y\right)} \frac{1}{k}\frac{\widehat{d}\left(k_x,k_y\right)}{\cosh(kh_0)} \\
&\quad \frac{1}{2\pi}\frac{i}{T}\int_{-\infty}^{\infty} d\omega e^{-i\omega t}\frac{1 - e^{i(\omega+i\epsilon_2)T}}{\omega + i\epsilon_2}\frac{(\omega^2 + i2\epsilon_1\omega)\sinh(kz) + g_0 k\cosh(kz)}{(\omega^2 + i2\epsilon_1\omega) - g_0 k\tanh(kh_0)} \\
&= \frac{1}{(2\pi)^2}\int_{-\infty}^{\infty}\int_{-\infty}^{\infty} dk_x dk_y\, e^{i\left(k_x x + k_y y\right)} \frac{1}{k}\frac{\widehat{d}\left(k_x,k_y\right)}{\cosh(kh_0)} \\
&\quad \frac{1}{2\pi}\frac{i}{T}\left[\int_{-\infty}^{\infty} d\omega \frac{e^{-i\omega t}}{\omega + i\epsilon_2}\frac{(\omega^2 + i2\epsilon_1\omega)\sinh(kz) + g_0 k\cosh(kz)}{(\omega^2 + i2\epsilon_1\omega) - g_0 k\tanh(kh_0)}\right. \\
&\qquad \left. - \int_{-\infty}^{\infty} d\omega \frac{e^{-i\omega(t-T)}e^{-\epsilon_2 T}}{\omega + i\epsilon_2}\frac{(\omega^2 + i2\epsilon_1\omega)\sinh(kz) + g_0 k\cosh(kz)}{(\omega^2 + i2\epsilon_1\omega) - g_0 k\tanh(kh_0)}\right].
\end{aligned} \tag{5.5A.7}$$

We first consider the integration in the second term:

$$\int_{-\infty}^{\infty} d\omega \frac{e^{-i\omega(t-T)}e^{-\varepsilon_2 T}}{\omega + i\varepsilon_2} \frac{(\omega^2 + i2\varepsilon_1\omega)\sinh(kz) + g_0 k\cosh(kz)}{\omega^2 + i2\varepsilon_1\omega - g_0 k\tanh(kh_0)}. \tag{5.5A.8}$$

Considering that the artificial damping is very small or the artificial damping parameters are much smaller than the angular frequency ω for tsunamis, we employ the residue theorem. The poles of Eq. (5.5A.8) are located at $\omega = -i\varepsilon_1 \pm \omega_0$ and $-i\varepsilon_2$ in the lower half of the ω-plane (Fig. 5.A.1), where

$$\omega_0 \equiv \sqrt{g_0 k\tanh(kh_0)}. \tag{5.5A.9}$$

When $t - T < 0$, we take the path of the integral in the upper half plane (path I in Fig. 5.A.1) including no poles. In this case, then, the integration is zero as

$$\int_{-\infty}^{\infty} d\omega \frac{e^{-i\omega(t-T)}e^{-\varepsilon_2 T}}{\omega + i\varepsilon_2} \frac{(\omega^2 + i2\varepsilon_1\omega)\sinh(kz) + g_0 k\cosh(kz)}{\omega^2 + i2\varepsilon_1\omega - g_0 k\tanh(kh_0)}$$
$$= 0 \quad \text{for } t - T < 0. \tag{5.5A.10}$$

When $t - T > 0$, we take the integral path in the lower half plane including the poles (path II in Fig. 5.A.1). By setting $\varepsilon_1 \to 0$, $\varepsilon_2 \to 0$ and using the residue theorem, we calculate Eq. (5.5A.8) as

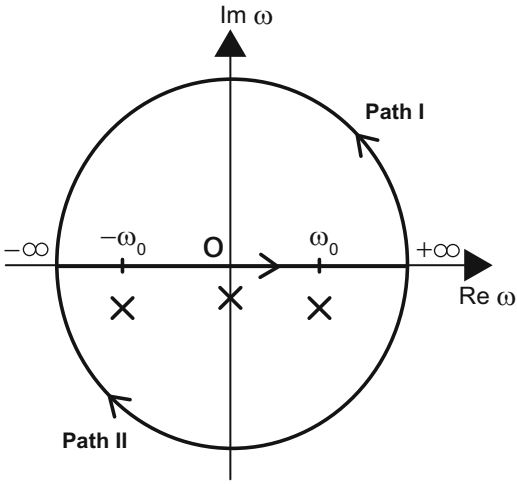

Fig. 5.A.1 Paths of integral in the complex ω-plane for Eq. (5.5A.8). The poles (crosses) are located at $\omega = -i\varepsilon_1 \pm \omega_0$ and $-i\varepsilon_2$ in the lower half plane

$$\begin{aligned}
&\int_{-\infty}^{\infty} d\omega \frac{e^{-i\omega(t-T)}e^{-\varepsilon_2 T}}{\omega+i\varepsilon_2}\frac{(\omega^2+i2\varepsilon_1\omega)\sinh(kz)+g_0k\cosh(kz)}{(\omega^2+i2\varepsilon_1\omega)-g_0k\tanh(kh_0)} \\
&\quad\approx \int_{-\infty}^{\infty} d\omega \frac{e^{-i\omega(t-T)}}{\omega+i\varepsilon_2}\frac{\omega^2\sinh(kz)+g_0k\cosh(kz)}{[\omega-(\omega_0-i\varepsilon_1)][\omega-(-\omega_0-i\varepsilon_1)]} \\
&\quad=-2\pi i[\mathrm{Res}(\omega=-i\varepsilon_2)+\mathrm{Res}(\omega=\omega_0-i\varepsilon_1)+\mathrm{Res}(\omega=-\omega_0-i\varepsilon_1)] \\
&\quad=-2\pi i\left[\frac{-g_0k\cosh kz}{\omega_0^2}+\frac{\omega_0^2\sinh kz+g_0k\cosh kz}{\omega_0^2}\cos\left[\omega_0(t-T)\right]\right]
\end{aligned} \tag{5.5A.11}$$

Summarizing Eqs. (5.5A.10) and (5.5A.11), we obtain

$$\begin{aligned}
&\int_{-\infty}^{\infty} d\omega \frac{e^{-i\omega(t-T)}}{\omega}\frac{\omega^2\sinh(kz)+g_0k\cosh(kz)}{\omega^2-g_0k\tanh(kh_0)} \\
&\quad=2\pi i\left[\frac{g_0k\cosh kz}{\omega_0^2}-\frac{\omega_0^2\sinh kz+g_0k\cosh kz}{\omega_0^2}\cos\left[\omega_0(t-T)\right]\right]H(t-T).
\end{aligned}$$

Using (5.5A.9), we have

$$\begin{aligned}
&\int_{-\infty}^{\infty} d\omega \frac{e^{-i\omega(t-T)}}{\omega}\frac{\omega^2\sinh(kz)+g_0k\cosh(kz)}{\omega^2-g_0k\tanh(kh_0)} \\
&\quad=2\pi i\left[\frac{\cosh kz}{\tanh kh_0}-\left(\frac{\cosh kz}{\tanh kh_0}+\sinh kz\right)\cos\left[\omega_0(t-T)\right]\right]H(t-T).
\end{aligned} \tag{5.5A.12}$$

The first term in the bracket in Eq. (5.5A.7) can also be calculated in a similar way. The velocity potential (5.5A.7) is then given by

$$\begin{aligned}
&\phi(x,y,z,t) \\
&=-\frac{1}{(2\pi)^2}\int_{-\infty}^{\infty}\int_{-\infty}^{\infty} dk_x dk_y\, e^{i\left(k_x x+k_y y\right)}\frac{\widehat{d}\left(k_x,k_y\right)}{k\cosh kh_0} \\
&\quad\left[\frac{\cosh kz}{\tanh kh_0}\frac{H(t)-H(t-T)}{T}\right. \\
&\qquad\left.-\left(\frac{\cosh kz}{\tanh kh_0}+\sinh kz\right)\frac{H(t)\cos\left(\omega_0 t\right)-H(t-T)\cos\left(\omega_0(t-T)\right)}{T}\right] \\
&=-\frac{1}{(2\pi)^2}\int_{-\infty}^{\infty}\int_{-\infty}^{\infty} dk_x dk_y\, e^{i\left(k_x x+k_y y\right)}\frac{\widehat{d}\left(k_x,k_y\right)}{k} \\
&\quad\left[\frac{\cosh kz}{\sinh kh_0}\frac{H(t)-H(t-T)}{T}\right. \\
&\qquad\left.-\left(\frac{\cosh kz}{\sinh kh_0}+\frac{\sinh kz}{\cosh kh_0}\right)\frac{H(t)\cos\left(\omega_0 t\right)-H(t-T)\cos\left(\omega_0(t-T)\right)}{T}\right]
\end{aligned} \tag{5.5A.13}$$

This equation is identical to Eq. (5.28).

Appendix 5B: Tsunami Propagation from an Initial Height Distribution and Zero Velocity Distribution

Setting the initial conditions as

$$\eta(x, y, t = 0) = \eta_0(x, y), \tag{5.5B.1}$$

and

$$\mathbf{v_H}(\mathbf{x}, t = 0) = 0, \text{and } v_z(\mathbf{x}, t = 0) = 0, \tag{5.5B.2}$$

the tsunami propagation is solved in the Cartesian coordinates (Fig. 5.B.1).

The velocity potential ($\mathbf{v} = \nabla\phi$) satisfies the Laplace equation (Eq. (5.3)):

$$\Delta\phi(\mathbf{x}, t) = 0. \tag{5.5B.3}$$

The velocity potential satisfies the boundary condition at the sea surface (Eq. (5.11)):

$$\left.\frac{\partial^2\phi(\mathbf{x}, t)}{\partial t^2}\right|_{z=0} + g_0 \left.\frac{\partial\phi(\mathbf{x}, t)}{\partial z}\right|_{z=0} = 0, \tag{5.5B.4}$$

and the boundary condition at the sea bottom:

$$\left.\frac{\partial\phi(\mathbf{x}, t)}{\partial z}\right|_{z=-h_0} = 0. \tag{5.5B.5}$$

Note that the initial conditions (Eqs. (5.5B.1) and (5.5B.2)) and the bottom boundary condition (Eq. (5.5B.5)) are different when compared with the tsunami generation problem treated in 5.2.1.

In order to solve this problem, we introduce the Fourier transform as

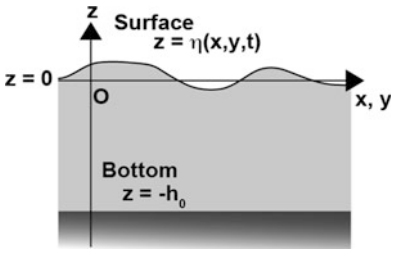

Fig. 5.B.1 Coordinates used in the formulation

$$\widehat{\phi}\left(k_x, k_y, z, t\right) = \int \int_{-\infty}^{\infty} dxdy\, e^{-i\left(k_x x + k_y y\right)} \phi(x, y, z, t). \tag{5.5B.6}$$

The corresponding inverse Fourier transform is

$$\phi(x, y, z, t) = \frac{1}{(2\pi)^2} \int \int_{-\infty}^{\infty} dk_x dk_y\, e^{i\left(k_x x + k_y y\right)}\, \widehat{\phi}\left(k_x, k_y, z, t\right). \tag{5.5B.7}$$

Then, the Laplace equation (Eq. (5.5B.3)) and the boundary conditions (Eqs. (5.5B.4) and (5.5B.5)) are rewritten as

$$\frac{d^2}{dz^2}\widehat{\phi}\left(k_x, k_y, z, t\right) = k^2 \widehat{\phi}\left(k_x, k_y, z, t\right), \tag{5.5B.8}$$

where $k^2 = {k_x}^2 + {k_y}^2$,

$$\left.\frac{\partial^2 \widehat{\phi}\left(k_x, k_y, z, t\right)}{\partial t^2}\right|_{z=0} + g_0 \left.\frac{\partial \widehat{\phi}\left(k_x, k_y, z, t\right)}{\partial z}\right|_{z=0} = 0, \tag{5.5B.9}$$

and

$$\left.\frac{\partial \widehat{\phi}\left(k_x, k_y, z, t\right)}{\partial z}\right|_{z=-h_0} = 0. \tag{5.5B.10}$$

The general solution of Eq. (5.5B.8) is given by

$$\widehat{\phi}\left(k_x, k_y, z, t\right) = A\left(k_x, k_y, t\right)\cosh(kz) + B\left(k_x, k_y, t\right)\sinh(kz). \tag{5.5B.11}$$

The coefficient $B(k_x, k_y, t)$ is represented by $A(k_x, k_y, t)$ by considering the bottom boundary condition (Eq. (5.5B.10)). Then, Eq. (5.5B.11) is calculated as

$$\widehat{\phi}\left(k_x, k_y, z, t\right) = A\left(k_x, k_y, t\right) \frac{\cosh[k(z + h_0)]}{\cosh(kh_0)}. \tag{5.5B.12}$$

Substituting (5.5B.12) into (5.5B.9), we obtain

$$\frac{d^2 A\left(k_x, k_y, t\right)}{dt^2} + \omega_0^2\, A\left(k_x, k_y, t\right) = 0, \tag{5.5B.13}$$

where

$$\omega_0^2 = g_0 k \tanh(kh_0). \tag{5.5B.14}$$

Equation (5.5B.14) represents the well-known dispersion relation (Eq. (3.47)). The general solution of Eq. (5.5B.13) is

$$A\left(k_x, k_y, t\right) = C\left(k_x, k_y\right)\cos\left(\omega_0 t\right) + D\left(k_x, k_y\right)\sin\left(\omega_0 t\right). \tag{5.5B.15}$$

Then, the velocity potential of Eq. (5.5B.11) is given by

$$\widehat{\phi}\left(k_x, k_y, z, t\right) = \left[C\cos\left(\omega_0 t\right) + D\sin\left(\omega_0 t\right)\right]\frac{\cosh[k(z+h_0)]}{\cosh(kh_0)}.$$

Considering the initial velocity condition of Eq. (5.5B.2), the coefficient of C needs to be zero:

$$\widehat{\phi}\left(k_x, k_y, z, t\right) = D\left(k_x, k_y\right)\sin\left(\omega_0 t\right)\frac{\cosh[k(z+h_0)]}{\cosh(kh_0)}. \tag{5.5B.16}$$

Then, the velocity potential is represented by the inverse Fourier transform as

$$\phi(x, y, z, t) = \frac{1}{(2\pi)^2}\int\int_{-\infty}^{\infty} dk_x dk_y\, e^{i\left(k_x x + k_y y\right)} D\left(k_x, k_y\right)\sin\left(\omega_0 t\right)\frac{\cosh[k(z+h_0)]}{\cosh(kh_0)}. \tag{5.5B.17}$$

The tsunami height is represented by the velocity potential as

$$\eta(x, y, t) = -\frac{1}{g_0}\frac{\partial\phi}{\partial t}\bigg|_{z=0}. \tag{5.5B.18}$$

By substituting (5.5B.17) into (5.5B.18), we get

$$\eta(x, y, t) = -\frac{1}{(2\pi)^2}\frac{1}{g_0}\int\int_{-\infty}^{\infty} dk_x dk_y\, e^{i\left(k_x x + k_y y\right)}\omega_0 D\left(k_x, k_y\right)\cos\left(\omega_0 t\right). \tag{5.5B.19}$$

Considering the initial tsunami height distribution (5.5B.1), we obtain

$$\widehat{\eta}_0\left(k_x, k_y\right) = -\frac{\omega_0 D\left(k_x, k_y\right)}{g_0},$$

or

$$D(k_x, k_y) = -\frac{g_0}{\omega_0}\widehat{\eta}_0(k_x, k_y), \tag{5.5B.20}$$

where $\widehat{\eta}_0(k_x, k_y)$ is the Fourier transform of the initial tsunami height distribution $\eta_0(x, y)$. Substituting Eq. (5.5B.20), we obtain the solution of the velocity potential as

$$\phi(x, y, z, t) = \frac{-1}{(2\pi)^2}\int\int_{-\infty}^{\infty} dk_x dk_y\, e^{i(k_x x + k_y y)} \frac{g_0}{\omega_0}\widehat{\eta}_0(k_x, k_y)\sin(\omega_0 t)\frac{\cosh[k(z+h_0)]}{\cosh(kh_0)}.$$

Using the dispersion relation (Eq. (5.5B.14)), we calculate

$$\phi(x, y, z, t) = \frac{-1}{(2\pi)^2} \times \int\int_{-\infty}^{\infty} dk_x dk_y\, e^{i(k_x x + k_y y)}\frac{\omega_0}{k}\widehat{\eta}_0(k_x, k_y)\frac{\cosh[k(z+h_0)]}{\sinh(kh_0)}\sin(\omega_0 t). \tag{5.5B.21}$$

Using the velocity potential of Eq. (5.5B.21), we can represent the velocity, the tsunami height, and the pressure change in the following.

$$\mathbf{v}_H(\mathbf{x}, t) = \nabla_H\phi(\mathbf{x}, t) = \frac{1}{(2\pi)^2}\int_{-\infty}^{\infty}\int_{-\infty}^{\infty} dk_x dk_y\, e^{i(k_x x + k_y y)}\widehat{\eta}_0(k_x, k_y) \left[-i\omega_0\frac{\mathbf{k}_H}{k}\frac{\cosh[k(z+h_0)]}{\sinh kh_0}\sin(\omega_0 t)\right], \tag{5.5B.22}$$

where $\nabla_H = (\partial/\partial x)\mathbf{e_x} + (\partial/\partial y)\mathbf{e_y}$, and $\mathbf{k}_H = k_x\mathbf{e_x} + k_y\mathbf{e_y}$.

$$\mathrm{v}_z(\mathbf{x}, t) = \frac{\partial\phi(\mathbf{x}, t)}{\partial z} = \frac{1}{(2\pi)^2}\int_{-\infty}^{\infty}\int_{-\infty}^{\infty} dk_x dk_y\, e^{i(k_x x + k_y y)}\widehat{\eta}_0(k_x, k_y) \left[-\omega_0\frac{\sinh[k(z+h_0)]}{\sinh kh_0}\sin(\omega_0 t)\right], \tag{5.5B.23}$$

$$\eta(\mathbf{x}, t) = -\frac{1}{g_0}\frac{\partial\phi}{\partial t}\bigg|_{z=0} = \frac{1}{(2\pi)^2}\int_{-\infty}^{\infty}\int_{-\infty}^{\infty} dk_x dk_y\, e^{i(k_x x + k_y y)}\widehat{\eta}_0(k_x, k_y)\cos(\omega_0 t), \tag{5.5B.24}$$

and

$$
\begin{aligned}
p_e(x,y,z,t) &= -\rho_0 \frac{\partial \phi(\mathbf{x},t)}{\partial t} \\
&= \frac{1}{(2\pi)^2} \int_{-\infty}^{\infty} \int_{-\infty}^{\infty} dk_x dk_y \, e^{i\left(k_x x + k_y y\right)} \rho_0 \widehat{\eta}_0\left(k_x, k_y\right) \\
&\quad \frac{\omega_0^2}{k} \frac{\cosh(z+h_0)}{\sinh(kh_0)} \cos\left(\omega_0 t\right).
\end{aligned}
\tag{5.5B.25}
$$

Using the dispersion relation (Eq. (5.5B.14)), we calculate

$$
\begin{aligned}
p_e(x,y,z,t) = &\frac{1}{(2\pi)^2} \int_{-\infty}^{\infty} \int_{-\infty}^{\infty} dk_x dk_y \, e^{i\left(k_x x + k_y y\right)} \\
&\rho_0 g_0 \widehat{\eta}_0\left(k_x, k_y\right) \frac{\cosh(z+h_0)}{\cosh(kh_0)} \cos\left(\omega_0 t\right).
\end{aligned}
\tag{5.5B.26}
$$

References

Aki K, Richards P (2002) Quantitative seismology. University Science Books, Sausalito

An C, Cai C, Zheng Y, Meng L, Liu P (2017) Theoretical solution and applications of ocean bottom pressure induced by seismic seafloor motion. Geophys Res Lett 44:10,272–10,281. https://doi.org/10.1002/2017GL075137

Ewing WM, Jardetzky WS, Press F (1957) Elastic waves in layered media. McGraw-Hill Book Company, Inc, New York

Filloux JH (1982) Tsunami recorded on the open ocean floor. Geophys Res Lett 9(1):25–28

Fujii Y, Satake K (2008) Tsunami sources of the November 2006 and January 2007 great Kuril earthquakes. Bull Seismol Soc Am 98(3):1559–1571. https://doi.org/10.1785/0120070221

Gill AE (1982) Atmosphere-ocean dynamics, International geophysics series, vol 30. Academic Press, New York

Gradshteyn IS, Ryshik IM (2000) Table of integrals, series and products (6th Ed. In Engl., ed. A. Jeffrey and D. Zwillinger). Academic Press, San Diego

Gusman AR, Tanioka Y, Sakai S, Tsushima H (2012) Source model of the great 2011 Tohoku earthquake estimated from tsunami waveforms and crustal deformation data. Earth Planet Sci Lett 341:234–242. https://doi.org/10.1016/j.epsl.2012.06.006

Hooper A et al (2013) Importance of horizontal seafloor motion on tsunami height for the 2011 Mw= 9.0 Tohoku-Oki earthquake. Earth Planet Sci Lett 361:469–479. https://doi.org/10.1016/j.epsl.2012.11.013

Ito Y et al (2011) Frontal wedge deformation near the source region of the 2011 Tohoku-Oki earthquake. Geophys Res Lett 38(7):L00G05. https://doi.org/10.1029/2011GL048355

Kajiura K (1963) The leading wave of a tsunami. Bull Earthq Res Inst 41:535–571

Kakinuma T, Akiyama M (2007) Numerical analysis of tsunami generation due to seabed deformation. Coast Eng 2006:1490–1502. https://doi.org/10.1142/9789812709554_0127

Kambe T (2007) Elementary fluid mechanics, vol 258. World Scientific, Singapore

Kennett BL (2001) The seismic Wavefield: volume I, introduction and theoretical development. Cambridge University Press, Cambridge

Kervella Y, Dutykh D, Dias F (2007) Comparison between three-dimensional linear and nonlinear tsunami generation models. Theor Comput Fluid Dyn 21(4):245–269. https://doi.org/10.1007/s00162-007-0047-0

Kubota T, Hino R, Inazu D, Ito Y, Iinuma T (2015) Complicated rupture process of the Mw 7.0 intraslab strike-slip earthquake in the Tohoku region on 10 July 2011 revealed by near-field pressure records. Geophys Res Lett 42(22):9733–9739. https://doi.org/10.1002/2015GL066101

Kubota T, Saito T, Suzuki W, Hino R (2017) Estimation of seismic centroid moment tensor using ocean bottom pressure gauges as seismometers. Geophys Res Lett 44:10,907–10,915. https://doi.org/10.1002/2017GL075386

Lotto GC, Nava G, Dunham EM (2017) Should tsunami simulations include a nonzero initial horizontal velocity? Earth Planets Space 69:117. https://doi.org/10.1186/s40623-017-0701-8

Murotani S, Iwai M, Satake K, Shevchenko G, Loskutov A (2015) Tsunami forerunner of the 2011 Tohoku Earthquake observed in the Sea of Japan. Pure Appl Geophys 172(3–4):683–697. https://doi.org/10.1007/s00024-014-1006-5

Nosov MA (1999) Tsunami generation in compressible ocean. Phys Chem Earth (B) 24(5):437–441

Nosov MA, Kolesov SV (2011) Optimal initial conditions for simulation of seismotectonic tsunamis. Pure Appl Geophys 168(6–7):1223–1237. https://doi.org/10.1007/s00024-010-0226-6

Okada Y (1985) Surface deformation due to shear and tensile faults in a half-space. Bull Seismol Soc Am 75(4):1135–1154

Pedlosky J (2013) Waves in the ocean and atmosphere: introduction to wave dynamics. Springer Science & Business Media, New York

Saito T (2013) Dynamic tsunami generation due to sea-bottom deformation: analytical representation based on linear potential theory. Earth Planets Space 65:1411–1423. https://doi.org/10.5047/eps.2013.07.004

Saito T (2017) Tsunami generation: validity and limitations of conventional theories. Geophys J Int 210(3):1888–1900. https://doi.org/10.1093/gji/ggx275

Saito T, Furumura T (2009) Three-dimensional tsunami generation simulation due to sea-bottom deformation and its interpretation based on the linear theory. Geophys J Int 178(2):877–888. https://doi.org/10.1111/j.1365-246X.2009.04206.x

Saito T, Tsushima H (2016) Synthesizing ocean bottom pressure records including seismic wave and tsunami contributions: toward realistic tests of monitoring systems. J Geophys Res Solid Earth 121(11):8175–8195. https://doi.org/10.1002/2016JB013195

Satake K, Kanamori H (1991) Abnormal tsunamis caused by the June 13, 1984, Torishima, Japan, earthquake. J Geophys Res Solid Earth 96(B12):19933–19939. https://doi.org/10.1029/91JB01903

Satake K, Fujii Y, Harada T, Namegaya Y (2013) Time and space distribution of coseismic slip of the 2011 Tohoku earthquake as inferred from tsunami waveform data. Bull Seismol Soc Am 103(2B):1473–1492. https://doi.org/10.1785/0120120122

Song YT, Mohtat A, Yim SC (2017) New insights on tsunami genesis and energy source. J Geophys Res Oceans 122:4238–4256. https://doi.org/10.1002/2016JC012556

Takahashi R (1942) On seismic sea waves caused by deformations of the sea bottom. Bull Earthq Res Inst 20:357–400

Tanioka Y, Satake K (1996) Tsunami generation by horizontal displacement of ocean bottom. Geophys Res Lett 23(8):861–864. https://doi.org/10.1029/96GL00736

Tanioka Y, Seno T (2001) Sediment effect on tsunami generation of the 1896 Sanriku tsunami earthquake. Geophys Res Lett 28(17):3389–3392

Tsushima H, Hino R, Tanioka Y, Imamura F, Fujimoto H (2012) Tsunami waveform inversion incorporating permanent seafloor deformation and its application to tsunami forecasting. J Geophys Res Solid Earth 117(B03311). https://doi.org/10.1029/2011JB008877

Yamamoto T (1982) Gravity waves and acoustic waves generated by submarine earthquakes. Soil Dyn Earthq Eng 1(2):75–82